

Controls on carbon dioxide and methane fluxes from a low-center polygonal peatland in the Mackenzie River Delta, Northwest Territories

June Skeeter, Andreas Christen, and Greg H.R. Henry

Abstract: Growing season surface–atmosphere exchange of carbon dioxide and methane were quantified at Fish Island, a wetland site in the lower northeast Mackenzie River Delta, Northwest Territories, Canada. The terrain consists of low-center polygonal tundra and is subject to infrequent flooding in high water years. Carbon dioxide and methane fluxes were continuously measured using eddy covariance and the relevance of different environmental controls were identified using neural networks. Net daily carbon dioxide uptake peaked in mid-July before gradually decreasing and transitioning to net daily emissions by September. Variations in light level and temperature were the main controls over diurnal net carbon dioxide uptake, whereas thaw depth and phenology were the main seasonal controls. Methane emissions measured at Fish Island were higher than comparable studies on river delta sites in the Arctic and were influenced by the interaction of a large number of factors including thaw and water table depth, soil temperatures, and net radiation. Spikes in methane emissions were associated with strong winds and turbulence. The Fish Island tundra was a net sink for carbon during the growing season and methane emissions only slightly reduced the overall sink strength.

Key words: carbon dioxide, methane, river delta, permafrost, peatland.

Résumé : Les échanges de dioxyde de carbone et de méthane entre la surface et l’atmosphère pendant la saison de croissance ont été quantifiés à Fish Island, une zone humide située dans le delta inférieur nord-est du fleuve Mackenzie, dans les Territoires du Nord-Ouest, au Canada. Le terrain consiste en une toundra polygonale concave et il est sujet à des inondations occasionnelles lors des années de hautes eaux. Les flux de dioxyde de carbone et de méthane ont été mesurés en continu par covariance des turbulences et la pertinence des différents contrôles environnementaux a été examinée à l’aide de réseaux neuronaux. L’absorption quotidienne nette de dioxyde de carbone a atteint un pic à la mi-juillet avant de diminuer progressivement et de passer à des émissions quotidiennes nettes en septembre. Les variations du niveau de lumière et de la température constituaient les principaux contrôles de l’absorption diurne nette de dioxyde de carbone, tandis que la profondeur de dégel et la phénologie constituaient les principaux contrôles saisonniers. Les émissions de méthane mesurées à Fish Island étaient plus élevées que celles d’études comparables sur des sites de deltas fluviaux dans l’Arctique et elles étaient influencées par l’interaction d’un grand nombre de facteurs, y compris le dégel et la profondeur de la nappe phréatique, les températures du sol et le rayonnement net. Les pics d’émissions de

Received 13 July 2021. Accepted 30 October 2021.

J. Skeeter and G.H.R. Henry.* Department of Geography, The University of British Columbia, Vancouver V6T1Z2, Canada.
A. Christen. Environmental Meteorology, Institute of Earth and Environmental Sciences, Faculty of Environment and Natural Resources, Albert-Ludwigs-Universität Freiburg, Freiburg, Germany.

Corresponding author: June Skeeter (e-mail: june.skeeter@ubc.ca).

*Greg H.R. Henry served as a Consulting Editor at the time of manuscript review and acceptance; peer review and editorial decisions regarding this manuscript were handled by Elyn Humphreys and Melissa Lafrenière.

© 2022 The Author(s). This work is licensed under a [Creative Commons Attribution 4.0 International License](https://creativecommons.org/licenses/by/4.0/) (CC BY 4.0), which permits unrestricted use, distribution, and reproduction in any medium, provided the original author(s) and source are credited.

méthane étaient associés à des vents forts et à de la turbulence. La toundra de Fish Island constituait un puits net de carbone pendant la saison de croissance et les émissions de méthane n'ont que légèrement réduit la force globale du puits. [Traduit par la Rédaction]

Mots-clés : dioxyde de carbone, méthane, deltas fluviaux, pergélisol, tourbière.

Introduction

The Canadian Arctic has experienced significant recent warming: mean annual temperatures increased 2.3 K from 1948 to 2016 (Zhang et al. 2019). Warming in the north is expected to accelerate with median estimates from CMIP5 suggesting an additional 2.1 K and 7.8 K by the 2080's under RCP2.6 and RCP8.5, respectively (Zhang et al. 2019). Warming has, and will continue to have, significant impacts across the Canadian Arctic, including permafrost degradation and increased active layer thickness, decreased snow cover and longer snow free seasons, changes in surface energy balance, and tundra greening (Derksen et al. 2019; Frost et al. 2020).

Approximately 500 Pg of carbon (C) is contained in the top meter of permafrost soils globally, with some of the highest concentrations in wetland areas, which are primarily located along river lowlands on river deltas (Hugelius et al. 2014). Climate change related disturbances put these shallow permafrost C stocks at risk for release into the atmosphere, as carbon dioxide (CO₂) and methane (CH₄) via aerobic and anaerobic respiration, respectively (Tarnocai et al. 2009; Hugelius et al. 2014; Schuur et al. 2015; Turetsky et al. 2020). Conversely, longer growing seasons, more liquid water availability, and consequently, enhanced plant growth, could have the opposite effect, increasing CO₂ uptake in some areas (Prowse et al. 2009).

The Mackenzie River Delta is the second largest Arctic delta after the Lena Delta in Siberia (Burn and Kokelj 2009) and is in one of the fastest warming regions in the world (Zhang et al. 2019; IPCC 2013). The Delta is a broad alluvial plain (12 000 km²) that grades from boreal forest in the south to low shrub tundra and sedge wetlands in the north (Burn and Kokelj 2009). Major Arctic delta lowlands, such as the Mackenzie River Delta, are important in the regional C-balance as they contain high C-stocks in a relatively small area (Schuur et al. 2015). Further, frequent flooding and water-saturated peatlands provide an environment particularly conducive to anaerobic conditions and hence CH₄ emissions. Despite its size and potential importance as a hotspot for C emissions, to date there has been little work done to quantify the C balance of the Mackenzie Delta. A series of airborne CH₄ flux observations in July of 2012 and 2013 provided delta-scale estimates of peak growing season methane emissions, but considerable spatial and interannual variability was observed (Kohnert et al. 2014). Delta-wide emissions were estimated to be 38 Gg CH₄ annually, with pockets of geologic strong emissions (>87 nmol·m⁻² s⁻¹) observed over discontinuous permafrost in the northwestern delta accounting for 17% of annual emissions (Kohnert et al. 2017). Kohnert et al. (2018) estimated fluxes from the boreal southern half of the delta and the tundra northern half to be 23 nmol·m⁻² s⁻¹ and 42 nmol·m⁻² s⁻¹ respectively. However, their estimates for the northern delta could be up to 40% geologic in origin (Kohnert et al. 2017). In situ observations of fluxes in the Mackenzie Delta are needed to put these airborne estimates in context, especially given the considerable emissions reported by Kohnert et al. (2017) for the northern portions of the delta.

This contribution reports field-scale measurements of CO₂ and CH₄ fluxes from a representative peatland site in the Northern Mackenzie River Delta. Net ecosystem exchange (NEE) of CO₂ and net methane exchange (NME) of CH₄ were measured at Fish Island, a

low-center polygonal peatland during the growing season and early senescent period using the eddy covariance (EC) approach (Aubinet et al. 2012) in 2017. NEE of CO₂ was calculated from fluxes and storage change and NEE was separated into ecosystem respiration (ER) and gross primary productivity (GPP), $NEE = ER - GPP$. NME was calculated from fluxes and storage change. The primary goals of our study were to: (1) measure growing season NEE and NME at Fish Island, (2) determine the main environmental drivers of CO₂ and CH₄ fluxes using neural network analysis, and 3) investigate the role of microtopography and landscape heterogeneity in driving the observed fluxes.

Materials and Methods

Study Site

The study took place at Fish Island (69°22′20.20″N, 134°52′51.92″W, WGS 84), which is located on the Big Lake Delta Plain in the northeastern part of the Mackenzie River Delta, Northwest Territories, Canada (Fig. 1). Fish Island is in the sparsely populated Inuvialuit Settlement Region, and the nearest communities are Tuktoyaktuk and Inuvik. The Big Lake Delta Plain is crisscrossed by a network of low-center ice wedge polygons and is subject to infrequent episodic flooding; sedimentation rates are low compared with western portions of the delta (Morse et al. 2012; Morse and Burn 2013). Fish Island (19 km²) is dominated by low-center polygons that are broadly representative of this portion of the delta. Permafrost under the Big Lake delta plain is continuous and thick (400 to 600 m), so we can expect CH₄ emissions observed in this area are strictly biogenic in origin (Kohnert et al. 2017). The Mackenzie Delta sits atop one of the largest oil and gas deposits in the Arctic (Gautier et al. 2009). Continuous permafrost acts as a cap, but there are sporadic strong natural gas emissions in the western portions of the delta where permafrost is discontinuous (Walter Anthony et al. 2012; Kohnert et al. 2017).

Vegetation at Fish Island varies with microtopography. The flat low-polygon centers make up the most land area and are covered by a dense mat of *Sphagnum* spp. moss along with *Equisetum* spp., and *Carex* spp. A patchwork of ridges ~10–20 cm high bound the polygon centers and hosted a more diverse mix of vegetation including a canopy of dwarf *Salix* spp. Degraded ridges form troughs 5–10 cm deep that are frequently ponded and host *Carex* spp. and *Eriophorum angustifolium* Honck. Fish Island is largely undisturbed with the exception of the defunct Taglu microwave tower, which has since been removed.

Data collection

A tripod equipped with an EC system was placed 400 m southeast of the river channel and 300 m northeast of Taglu tower on Fish Island. EC measurements were done from 0:00 day of year (DOY) 174 (23 June) to 12:30 DOY 256 (13 September) 2017 and drone imagery was collected on DOY 174, 191, 233, and 256 using a Phantom 3 drone (DJI, Shenzhen, China). The drone images were used to map the study site and monitor vegetation change in the vicinity of the EC station though the study period (Fig. 2). The imagery was processed using Open Drone Map (2020) to create georeferenced 10 cm resolution orthophotos for each date. The orthophotos were used to create a landscape classification by manually digitizing the boundaries between microtopographic features within a 150 m radius of the EC tower. The landscape classification was then converted to a 2 m resolution raster image centered on the tripod, henceforth referred to as the landscape classification map (LCM), to match the resolution of the flux footprint analysis (discussed in the EC fluxes section).

A sensitivity analysis was conducted to assess spatial variability within the LCM and estimate the distribution of LCM classes. A random sample of points ($n = 100$) were generated within the 150 m radius of the EC tower, and the proportion of points falling within each LCM class was calculated. This was repeated 2501 times (equivalent to the number of CO₂

Fig. 1. False color composite 100 m resolution LANDSAT8 image (bands 3, 4, and 5) of the Mackenzie Delta with imagery spanning the dates of the 2017 study period. Labeled on the map are the study site at Fish Island and the nearby communities of Tuktoyaktuk and Inuvik. The approximate bounds of the Big Lake Delta Plain are represented with the white hatch marks (Morse and Burn 2013). Coordinate Reference System: NAD83 UTM zone 10N. LANDSAT8 data is provided by the United States Geological Survey and was downloaded using Google Earth Engine.



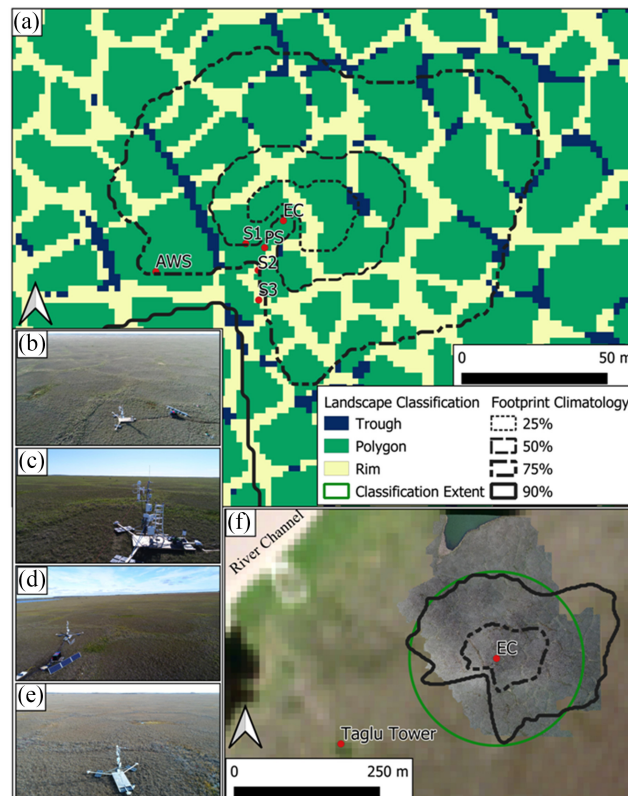
flux samples) and used to calculate the mean landscape fraction (LF) of each class with a 95% confidence interval. The LF for polygon centers, rims, and troughs, were 66.1 ($CI_{95\%} \pm 0.3$), 28.7 ($CI_{95\%} \pm 0.2$), 5.1 ($CI_{95\%} \pm 0.3$) % respectively.

Since 2008 there has been an automatic weather station (AWS) at the site operated by the Northwest Territories Water Resources Department recording temperature, radiation, wind speed and direction, snow depth, and rainfall (NWT Water Resources 2019). Mean annual air temperature (T_a) over the last decade (August 2008 – July 2019) was -8.5 °C, whereas the 30 year (1980–2010) climate normal at Tuktoyaktuk (60 km east) was -10 °C (Environment Canada 2016). Over the ten years at Fish Island, July was the warmest month with a mean of 11.6 °C and January was the coldest at -24.5 °C. Mean annual precipitation was 117 mm·yr $^{-1}$, with the majority falling as rain in the summer and autumn. Snow cover typically lasts from late September or October to late May.

EC fluxes

The EC system measured fluxes of CO_2 (F_{CO_2}) and CH_4 (F_{CH_4}) over the study period. It consisted of a closed-path infrared CO_2/H_2O gas analyzer (IRGA, model LI-7200, LI-COR Inc., Lincoln, NE, USA; LI-COR), an open-path CH_4 analyzer (model LI-7700, LI-COR), and a

Fig. 2. (a) The cumulative flux footprint climatology (25%, 50%, 75% and 90%) is shown overlain on the landscape classification map (LCM). Labels on the map correspond to: the eddy covariance system (EC), soil stations 1–3 (S1, S2, S3), the power supply (PS), and the Northwest Territories Water Resource Department’s Automated Weather Station (AWS). (b–e) Oblique drone photos showing the EC system and vegetation at different points during summer and fall 2017: (b) looking southeast on DOY 174 and (c) DOY 191 and looking northeast from behind the EC system on (d) DOY 233 and (e) DOY 256. (f) Inset map showing the location of the EC station, 75% and 90% flux footprint contours and the area covered by the LCM, and a 10 cm orthophoto created from drone imagery captured on 23 June. This is overlain on a 10 m resolution composite Sentinel 2 image generated using Google Earth Engine with imagery spanning the summer 2020. Also shown are the location of the Taglu tower and the River Channel. Coordinate Reference System: NAD83 UTM zone 10N. Sentinel 2 data is provided by the Copernicus Sentinel Data and was downloaded using Google Earth Engine.



CSAT3 sonic anemometer (Campbell Scientific Inc, Logan, UT, USA; CSI) mounted on a tripod at a measurement height (z_m) of 2.87 m (Fig. 1). The EC data and air pressure (P_a) were logged on a LI-7550 Analyzer Interface Unit (LI-COR). The CSAT3 was oriented to the northeast (35°) because northerly and easterly winds are most common for this time of year (NWT Water Resources 2019). Due to an error setting up the LI-7550, fluxes were only logged at 1 Hz until 12:00 DOY 193; the settings were corrected after this and the fluxes were logged at 10 Hz for the remainder of the study period. In principle, the low sampling frequency does not cause a bias in the mean flux, but does increase the variance (Bosveld and Beljaars 2001). This is supported by experimental observations (Rinne et al. 2008; Holl et al. 2019). To confirm this error had limited impact on our results we down sampled the July flux data for the period following the error correction (13–29 July). We artificially generated a 1 Hz data set by selecting every tenth value from the raw data, and processed it using the same steps as detailed below. Student’s t tests indicated no significant difference between

the mean values of the 10 Hz data and the down sampled 1 Hz data for either CO₂ or CH₄ fluxes. Boxplots of the results 1 and 10 Hz fluxes are shown in Supplementary Fig. S1¹.

Half-hourly fluxes were calculated with EddyPro V.6.2.0 (LI-COR). The software performed statistical assessments (Vickers and Mahrt 1997), low and high frequency spectral corrections (Moncrieff et al. 1997 and 2004), and a double rotation (Wilczak et al. 2001). For the open path LI-7700, the Webb, Pearman, and Leuning (WPL) density correction was applied (Webb et al. 1980) with spectroscopic correction following McDermitt et al. (2011). For the closed path LI-7200 density corrections were calculated following Ibrom et al. (2007). Quality control flags (0–2) were assigned following Mauder and Foken (2004) and fluxes with a flag of 2 were discarded (4.6% and 10.8% of F_{CO_2} and F_{CH_4} data, respectively).

Post processing treatments were conducted as follows. (1) Removing LI-7700 observations during precipitation events (0.2% of F_{CH_4} data). (2) Removing LI-7700 observations when signal strength (received signal strength indicator, RSSI) from the LI-7700 was below 20% (13.3% of all data). Methane concentrations and F_{CH_4} were plotted against RSSI to confirm this was an acceptable threshold (Supplementary Fig. S2¹). Low RSSI values can result from condensation or dust on the mirror of the LI-7700. We elected not to use a cleaning pump at this site because of the limited power supply. This resulted in more missing F_{CH_4} data but extended the lifespan of the power supply for measuring fluxes. (3) Removing observations with mean wind direction from $215^\circ \pm 30^\circ$ (8.3% and 7.1% of F_{CO_2} and F_{CH_4} data, respectively) to avoid uncertainties associated with the wake of the sonic anemometer. (4) Storage correcting by calculating net fluxes (NEE and NME) as the sum of the observed scalar flux (F_{CO_2} and F_{CH_4}) and the rate of change in their scalar concentrations at z_m following Aubinet et al. (2012). (5) Removal of spurious half-hourly measurements (4.1% and 3.3% of NEE and NME data, respectively) using the median absolute deviation about the median method following Papale et al. (2006). (6) Filtering fluxes by friction velocities (u_*) below an 0.1 m s^{-1} (4.4% and 2.3% of NEE and NME data). We confirmed that this value was suitable by calculating an iteratively determined u_* threshold (0.094 m s^{-1}) following Papale et al. (2006). In total, quality control and post processing removed 22% and 55% of F_{CO_2} and F_{CH_4} observations, respectively. Additionally, there was a 14 day gap in flux observations from 00:30 DOY 240 to 16:30 DOY 254 due to insufficient power supply from the solar panels. The CSAT3 and climate station remained operational, but the Li-7200 and Li-7700 were shut down.

The flux footprint was calculated following Kljun et al. (2015). All variables needed for footprint calculations were collected onsite, except planetary boundary layer height. Inverse distance weighting was used to interpolate these values from 3 hour reanalysis data for the 25 nearest grid points spanning the domain $68^\circ 30' \text{N}$ to 70°N and 134°W to $135^\circ 40' \text{W}$. Half-hourly values were then approximated from the 3 hour value using linear interpolation. The flux footprint was calculated at a spatial resolution of 2 m^2 over a $2000 \text{ m} \times 2000 \text{ m}$ grid centered on the tripod for all valid half-hourly measurement periods: $u_* > 0.1 \text{ m s}^{-1}$ and mean wind direction $\neq 215^\circ \pm 30^\circ$. The half-hourly footprints were intersected with the landscape classification to determine the relative flux contribution of low-center polygons (F_{Cnt}), rims (F_{Rim}), and troughs (F_{Tro}) to each measurement. The contribution from outside the landscape classification (F_{Out}) was calculated as $1 - (F_{Cnt} + F_{Rim} + F_{Tro})$. To allow for a direct comparison with the source area fractions, the LF values weighted by $(1 - F_{Out})$, using the median value of F_{Out} to calculate the adjusted landscape fraction (ALF).

Neural networks (NN) were used to identify relevant environmental controls over NEE and NME, gap fill the time series, and partition NEE into its component fluxes ER and

¹Supplementary data are available with the article at <https://doi.org/10.1139/as-2021-0034>.

GPP. Various studies have applied NNs to flux data to identify and analyze flux drivers (Moffat et al. 2010; Briegel et al. 2020; Skeeter et al. 2020), investigate the influence of spatial heterogeneity (Morin et al. 2014; Skeeter et al. 2020), and to gap-fill time series of NEE and NME (Papale and Valentini 2003; Dengel et al. 2013; Knox et al. 2016; Skeeter et al. 2020). The steps for identifying relevant controls, gap filling, and flux partitioning are discussed in the Feature identification and gap-filling section.

Weather and soil measurements

Climate data at the EC site were logged on a CR1000 datalogger every 1 s and averages/totals stored at 5 minute intervals. A NRLite net radiometer (Kipp & Zonen, Delft, Netherlands) measured net all-wave radiation (R_n) and a SQ-110 quantum sensor (Apogee Instruments, Logan, UT, USA) measured photosynthetic photon flux density (PPFD) at 3 m a.g.l, and a HMP35 (CSI) measured T_a and humidity (RH) in a shielded, naturally ventilated screen all at 2 m a.g.l. on the same tripod as the EC system. A tipping bucket rain gauge (R.M Young Company, Travers City, MI, USA) was mounted 2 m south of the tripod at a height of 0.4 m.

Soil temperature, moisture, and water table depth data were recorded at 30 minute intervals on three separate, automatic soil sites, each operated by a CR10x datalogger (CSI) at three locations near the tripod (Fig. 2a): one in polygon a center (S1), one on a polygon rim (S2), and one on a border between the rim and the center (S3). At each of the soil sites, soil temperatures (T_s) were recorded with custom made type-T thermocouples at depths of 2.5, 5, and 15 cm, volumetric water content (θ_w) was measured with CS616 water content reflectometers (CSI) at 0.1 m depth, and water table depth (W_{td}) was sampled with PLS probes (CSI). The climate and soil stations S1 and S2 operated uninterrupted from 23 June (DOY 175) until 13 September 2017 (DOY 257). On 17 July an animal dug up and destroyed the thermocouples and CS616 at S3. The PLS probes were installed at the base of the active layer and adjusted to account for increasing thaw depth on 10 July and 1 August. Thaw depth (TD) was measured during each site visit by inserting a graduated steel probe into the ground to point of refusal. Thaw depths were measured ten times for both polygon rims and centers and the median value calculated for each set of observations. Canopy heights were also measured for polygon rims and centers on each site visit using the median value of 10 replications.

The sun remains above the horizon much of the summer at 69°N. The date of the first sunset and timing subsequent sunrises and sunsets is important for understanding NEE and partitioning GPP and ER. We obtained the timing of sunrises and sunsets from a sunrise/sunset calculator (National Research Council Canada 2012). We used this information to one-hot encode a *Daytime* variable. Every half-hourly measurement period occurring before the first sunset or between sunrise and sunset was assigned a value of one. Measurements between sunset and sunrise were assigned a value of zero. If a sunrise or sunset occurred during a measurement period, the encoding was set to 1, as the purpose of this coding is to identify periods with no GPP.

Chamber measurements

In addition to EC measurements, ER was independently measured using the closed chamber method on two site visits (DOY 191, and DOY 233). Closed chamber measurements were sampled using a LI-700 (LI-COR) mounted in a custom made portable automated chamber as described by Christen et al. (2017). ER was measured at polygon centers (ER_{Cnt}) and rims (ER_{Rim}) using eight and four replications, respectively. Opaque PVC collars were inserted 10 cm into the ground on DOY 173. Before each measurement, chamber heights were measured with four repetitions per collar. Then the transparent PVC sensor head

was placed over the collar and covered with an opaque canvas bag to block out all sunlight. The sampling period lasted 2 min and fluxes were then calculated following [Christen et al. \(2017\)](#). Due to limited time and resources, we were only able to collect a small number of samples and we were unable to collect chamber observations of GPP. The small sample size limits the conclusions we can draw from the chamber data, but this data are still valuable because they provide context to our EC observations and allow for comparison with other sites.

Feature identification and gap-filling

Neural networks

NN are flexible machine learning methods that make no prior assumptions about functional relationships within a data set and are ideally suited to perform non-linear, multi-variate regression ([Hornik 1991](#); [Melesse and Hanley 2005](#); [Desai et al. 2008](#)). The goal of a NN is to approximate a target function as:

$$(1) f(X, w) = t(X) - \varepsilon(X)$$

where $t(X)$ is the target (e.g., NEE's response to environmental drivers), $\varepsilon(X)$ the noise, and $X = [x_0, x_1, \dots, x_M]$ is the set of input variables; M denotes the number of input variables, and $x_0 = 1$ is a bias term ([Khosravi et al. 2011](#)). In the context of EC measurements, this means that if all relevant climate and ecosystem information are available to a network, the remaining variability can be attributed to noise in the measurement ([Moffat et al. 2010](#)).

Here, we used feed-forward dense NN with a single hidden layer:

$$(2) f(X, w) = \sum_{h=1}^H \beta_h g\left(\sum_{m=0}^M \gamma_{hm} x_m\right)$$

Where $g(\cdot)$ is a non-linear transfer function, here we used the rectified linear activation unit (ReLU) ([Anders and Korn 1999](#)). H denotes the number of hidden nodes in the network. The weights $w = [\beta_1 \dots \beta_H, \gamma_{10} \dots \gamma_{HM}]$ are randomly initialized and after each model iteration are updated by backpropagating the error through the network, β are the weights of the output layer and γ are the weights of the hidden layer. Weights are adjusted in the direction that decrease the error and training continues. We used early stopping to terminate training when the mean squared error (MSE) of a test data set failed to improve for 10 consecutive iterations. The test set consisted of 10% of the training data, and was not used if fitting $f(X, w)$. Early stopping prevents $f(X, w)$ from overfitting the training data ([Weigend and Lebaron 1994](#); [Sarle 1995](#); [Tetko et al. 1995](#); [Sarle 2014](#)). When using early stopping, the choice of H is somewhat arbitrary, but H must be large enough to ensure the model has sufficient flexibility ([Sarle 2014](#)). We set H to $1/30^{\text{th}}$ the number of training samples.

To account for the random initialization of w and further minimize overfitting, stratified bootstrapping (with replacement) was used to generate a set of 30 bootstrapped training data sets (B). Separate $f(X, w)_i$ were trained on each bootstrapped training set and for each model and validation metrics: root mean squared error (RMSE) and the coefficient of determination (r^2) were calculated using the out of bag (OOB) bootstrapped samples. Thus, the final response model response was calculated as:

$$(3) F(X) = \frac{1}{B} \sum_{b=1}^B f_b(X, W)$$

where $F(X)$ is the response of NEE or NME to a set of inputs (environmental drivers). The variance of the model outputs is:

$$(4) \quad \sigma^2(X) = \frac{1}{B-1} \sum_{b=1}^B (f_b(X, W) - F(X))^2$$

A confidence interval (CI) for $F(X)$ can be calculated as $F(X) \pm t_{(1-\alpha, df)} \sigma(X)$, where $t_{(1-\alpha, df)}$ is the students t score, $1-\alpha$ is the desired confidence level, and df are the degrees of freedom that are set to the number of bootstrapped samples B .

The weights method

Our NN analysis used the Weights method (Gevrey et al. 2003) to quantify the relative influence of various inputs on NEE and NME and to prune the NN to reduce the number of input variables. This method has been used to study the influence of inputs for ecological modelling (Lee et al. 2003; Olden, et al. 2004; Fischer 2015; Liyanaarachchi et al. 2020), but to our knowledge, it has yet to be applied to EC flux data. For both NEE or NME, $F(X)$ were initially trained on 21 initial inputs X including: radiation (R_n , $PPFD$, $Daytime$), atmospheric conditions (T_a , vapor pressure deficit (VPD), P_a), wind (U , u), flux contribution (F_{Cnt} , F_{Rim} , F_{Tro}), and sub-surface (T_s (all depths, polygon center and rim), VWC (polygon center and rim), water table depth (W_{TD}), thaw depth (TD)) variables. These X were chosen because they potentially influence NEE or NME.

After training, we calculated the partial derivatives (d_{ji}) of each input factor x_m in X for every sample ($j=1, \dots, N$), where N is the total number of flux observations:

$$(5) \quad d_{jm} = S_j \sum_{h=1}^H \beta_h \gamma_{mh} \max \begin{cases} 0, & I_{hj} \leq 0 \\ 1, & I_{hj} > 0 \end{cases}$$

where S_j is the derivative of the output with respect to the input, β_h and γ_{mh} are the weights of the output and hidden neurons, and I_{hj} is the response of the of the h^{th} hidden neuron for the input $x_{j,m}$. The max function is the first derivative of the ReLu activation function. d_{ji} were averaged over the bootstrapped data sets and plotted to visualize the influence of factors. Because the inputs and the target must be standardized (mean = 0, standard deviation = 1) before training a NN, d_{ji} are not in the units of NEE or NME, rather they can be interpreted in terms of relative magnitude (i.e., compared between inputs). When $d_{ji} < 0$ the respective input has a negative influence on the target and when $d_{ji} > 0$ it has a positive influence.

Next, the sum the of partial derivatives (SD_m) and sum of the squared partial derivatives were calculated (SSD_m) for each input m :

$$(6) \quad SD_m = \sum_{j=1}^J d_{ji}$$

$$(7) \quad SSD_m = \sum_{j=1}^J (d_{ji})^2$$

The sign of the S_{Dm} indicates whether the variable has a net positive or negative influence on the output (over the input domain). The SS_{Dm} describes the relative magnitude of the variables influence (if d_{ji} changes sign, S_{Dm} is reduced but SS_{Dm} is not). The SS_{Dm} values for each input were then normalized by the sum of all SSD values to quantify the relative influence (RI) of each input factor. The 21-input model served as a benchmark to gauge the performance of a “pruned” model using only the inputs X with over 2.5% influence. Amiri et al. (2020) suggest removing inputs that have less than a 5% influence on the model; we used twice as many initial inputs as they did, so we chose 2.5%. The SS_{Dm} of the pruned

models were calculated and used to gauge the relative influence of the flux drivers. Additionally, the partial derivatives for some of the most important drivers were plotted to visualize their relative influence.

The $B = 30$ pruned models for both NEE and NME were then run on the time series of drivers over the full study period. The 30 bootstrapped model outputs were averaged and used to estimate mean NEE and NME by gap-filling the NEE and NME time series. Most drivers just had nearly complete records (>99%); brief gaps in the drivers were gap-filled with linear interpolation (up to 60 minutes). Wind speed and u_* had slightly more missing records (99% and 98% complete, respectively) and were also gap-filled with linear interpolation. The footprint drivers had more missing values (95% complete), F_{Cnt} , F_{Rim} , and F_{Tro} were gap-filled using their respective mean values, binned by wind direction in 10° intervals. Confidence intervals for NEE and NME were calculated using the total variance of multiple imputations, which is the sum of variance between and within imputations.

Partitioning NEE

Typically, NEE is gap-filled using flux-partitioning algorithms that model ER using T_s or T_a and GPP using $PPFD$ (e.g., Aubinet et al. 2012; Lee et al. 2017) where $NEE = ER - GPP$. However, these methods require nighttime observations to estimate ER and, thus, do not perform well for Arctic summertime measurements due to the limited number of samples available during low light conditions (Kutzbach et al. 2007; Runkle et al. 2013). We tested a Q10 T_a response curve (eq. 9.4 in Aubinet 2012) and a logistic T_s response curve (eq. 1 in Lee et al. 2017) using each of the six T_s measurements to gauge their effectiveness when trained on the limited number ($n = 186$) of ER samples.

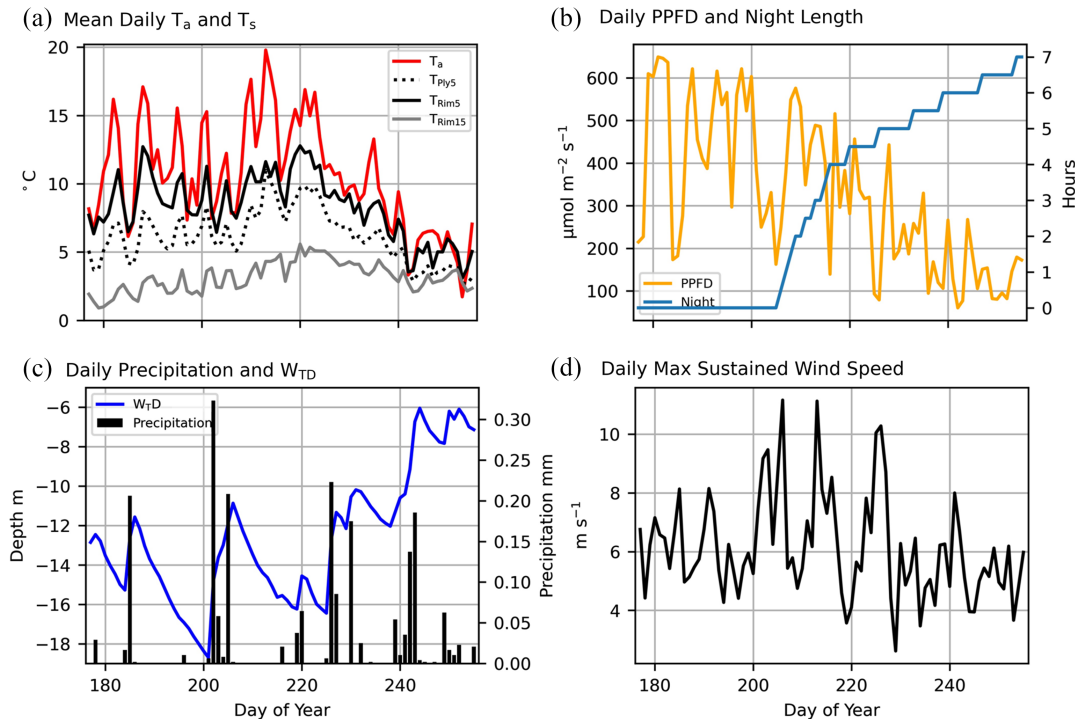
A NN trained on CO_2 fluxes will just estimate NEE rather than the component fluxes ER and GPP. To compensate for this, we estimated daytime ER with the pruned NN by using an artificial “dark” input set (Skeeter et al. 2020). The inputs *Daytime* and *PPFD* were both set to zero and any $R_n > 0$ were also set to zero. This approximation projects ER well beyond conditions under which it was actually observed, so caution needs to be taken when interpreting the output. However, the NN performed better than the traditional methods when estimating nighttime ER (see Ecosystem respiration section). Therefore, we feel this is the best option for estimating ER and is useful for comparing to the ER chamber observations. The ER estimate and confidence interval were obtained by “gap-filling” the sparse record of nighttime NEE ($n = 186$) observations using the same procedure as for NEE and NME.

Results

The spring flood peaked on 1 June in 2017 at the nearby (4 km) Big Lake gauge station (Environment Canada 2020). It is unclear whether the site was inundated during the flood, but satellite imagery indicated Fish Island was snow free by 1 June. Vegetation had started to turn green at the onset of the study period, but was still mostly brown (Fig. 2b). A rapid green-up occurred over the first couple weeks of the study period. Vegetation height increased from 8 to 14 cm in the polygon centers and 13 to 23 cm on polygon rims between 23 June and 21 August after which it did not change appreciably. Thaw depths increased steadily from 20 cm (DOY 174) to 50 cm (DOY 256) for polygon centers and was consistently 2 cm deeper for polygon rims.

Compared with the same dates (23 June to 13 September) from the AWS record on Fish Island (2009–2018) the 2017 study period was the third warmest and second wettest on record. Over the 82 day study, T_a ranged between -0.1 and 24.8 °C and mean T_a was 10.6 °C (Fig. 3a). Soil temperatures peaked in August before decreasing along with a decline in daily R_n . Polygon rim T_s were warmer than centers at all depths, and the difference was most pronounced at 5 cm depth with a mean difference of 2.3 °C. $PPFD$ was highly variable day to day

Fig. 3. Climate and water level measurements during the 2017 study period: (a) Daily mean T_a in red and daily mean T_s at 5 cm for polygon centers (dotted line), rims at 5 cm (solid black line), and rims at 15cm (solid grey line). (b) Mean daily photosynthetic photon flux density (PPFD) and length of each night after the first sunset. (c) Total daily precipitation (black bars) and mean daily water table depth (W_{TD}) (blue line). (d) Daily maximum sustained half-hourly wind speed at 2.89 m (black line).



depending on cloud conditions and decreased through the study period (Fig. 3b). The first sunset was on DOY 206 (25 July), after which the day length began to rapidly decrease. Precipitation during the study period (100 mm) fell on 33 days contributing to the near-record wet conditions in 2017. The water table depth in polygon centers averaged 13 cm below the surface, ranging from 19 cm in July to 5 cm in September (Fig. 3c). The base of the active layer under polygon rims was above the water table until 21 July, after which a perched water table formed.

The flux footprint climatology is shown in Fig. 2a. Analysis of half-hourly footprints indicates that the source area of NEE and NME observations were predominately sourced from within the LCM, median F_{Out} was 10.9% and 11% for NEE and NME, respectively. Relative to the ALF, F_{Cnt} tended to be slightly overrepresented, whereas F_{Rim} and F_{Tro} were slightly underrepresented, but they were all within the interquartile range (Table 1). A chi square test ($\chi^2 = 3.58$, $p = 0.61$) indicated the median values of F_{Cnt} , F_{Rim} , and F_{Tro} were not significantly different than the expected ALF values. Wind speeds were highly variable and there were multiple strong storm events with gusts up to $30 \text{ m}\cdot\text{s}^{-1}$ (see Fig. 3d). The 2017 study period had the second highest average wind speed on the AWS record.

Seasonal and daily trends

Figure 4 shows the course of observed NEE and NME and daily gap-filled NEE and NME over the study period. During the entire study period, Fish Island was a net sink for CO_2 with mean NEE of -0.60 ($\text{CI}_{95\%} \pm 0.04$) $\mu\text{mol}\cdot\text{m}^{-2}\cdot\text{s}^{-1}$. Day to day NEE varied depending on

Table 1. Descriptive statistics of the source area for half-hourly net methane exchange (NME) observations. Despite net ecosystem exchange (NEE) having over 1,000 more half-hourly observations, the quantiles for NEE were nearly identical ($\pm 1\%$). Column headers for the landscape class flux contributions show their fractional cover in landscape classification map. The adjusted landscape fraction (ALF) values shown at the bottom are the landscape fraction (LF) estimates weighted by $(1 - F_{Out})$, using the 50th percentile value of F_{Out} .

	F_{Cnt}	F_{Rim}	F_{Tro}	F_{Out}
Minimum	33.0%	5.1%	0.0%	7.3%
25th percentile	58.7%	20.6%	1.8%	10.5%
50th percentile	62.8%	22.4%	3.4%	11.0%
75th percentile	63.7%	28.3%	4.8%	11.4%
Maximum	77.5%	56.4%	9.4%	18.1%
ALF	58.8%	25.6%	4.6%	N/A

Fig. 4. Daily measured (a) net ecosystem exchange (NEE) and (b) net methane exchange (NME) (boxplot) and mean gap-filled (black line) (a) NEE and (b) NME over the study period. For the boxplots, the red line indicates the median, the red square is the mean, the box represents the inner quartile range (Q1–Q3), the whiskers are 1.5 times the inner quartile range ending at the farthest data point within that interval, and circles represent outliers. Grey shading represents a net sink and no shading represents a net source.

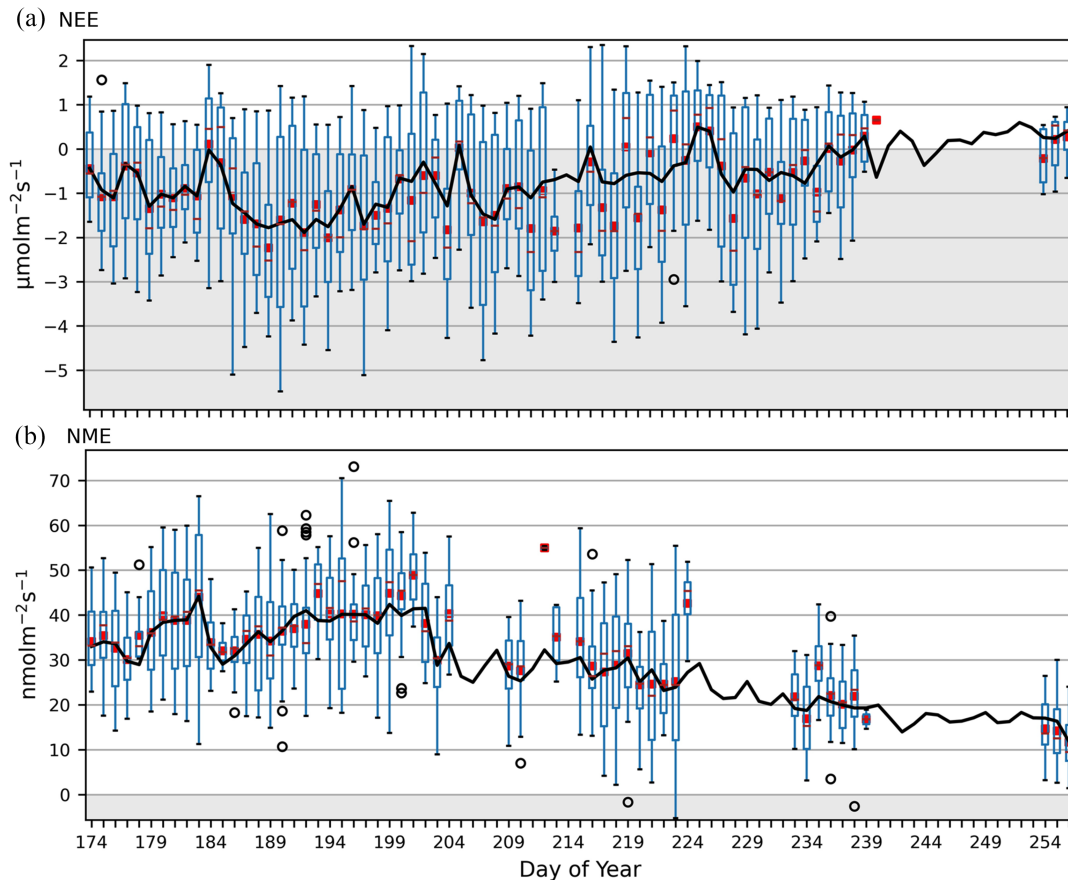
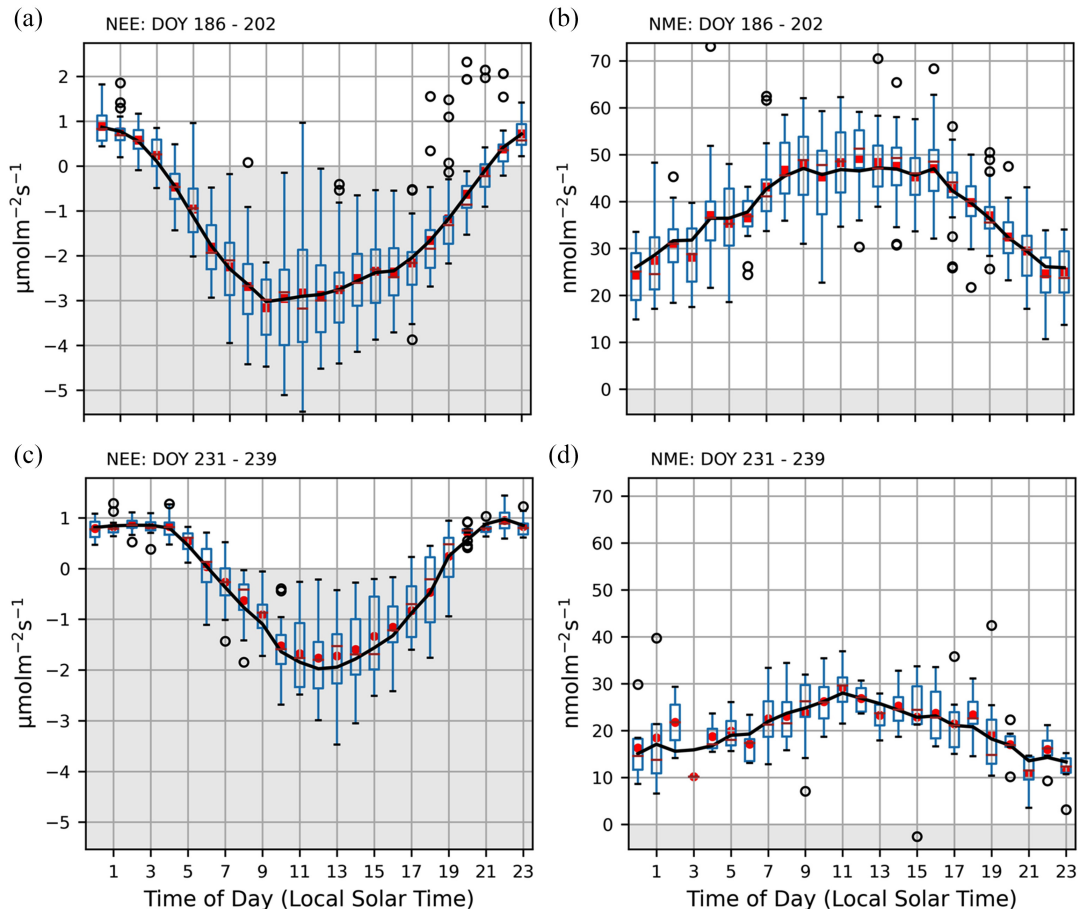


Fig. 5. Diurnal (hourly) course of measured net ecosystem exchange (NEE) and net methane exchange (NME) (boxplot) and mean gap filled (black line) NEE and NME early in the study period (*a* and *b*) and late in the study period (*c* and *d*). For the boxplots, the red line indicates the median, the red square is the mean, the box represents the inner quartile range (Q1–Q3), the whiskers are 1.5 times the inner quartile range ending at the farthest data point within that interval, and circles represent outliers. Grey shading represents a net sink and no shading represents a net source.



cloud conditions. CO₂ uptake increased during the early season until peaking in early–mid July (DOY 190) as vegetation matured (Fig. 2c). Net CO₂ uptake remained high through July, then as day length and sun angle decreased through August. The site became a net CO₂ source by the end of the study period as plant life senesced (Figs. 2d and 2e).

The site was a net CH₄ source during the study period with mean NME of 27.7 (CI_{95%} ± 0.35) nmol·m⁻² s⁻¹. Day to day NME was less variable than NEE, but there were significant spikes associated with high wind events (discussed below). Methane emissions increased slightly through the beginning of the study period, peaking on DOY 202 then abruptly decreasing. Through the rest of the period, NME was consistently lower and continued to decrease through September. Light precipitation, condensation, and fog were common in the latter half of the study period, resulting in a large number of missing observations from this period due to low RSSI values.

Figures 5a and 5b shows the daily cycle of CO₂ and CH₄ exchange for the period when both CO₂ uptake and CH₄ emission were greatest. During this period, NEE was negative

Table 2. The relative influence (RI) of the inputs of the pruned neural network (NN) over net ecosystem exchange (NEE), along with their correlation (r) to half-hourly NEE.

Rank	Symbol	Factor	RI	Sign	r
1	<i>PPFD</i>	Photosynthetic photon flux density	64%	–	–0.79
2	<i>VPD</i>	Vapour pressure deficit	8%	–	–0.44
3	T_{Cnt5}	Soil temperature 5 cm, polygon centers	7%	+	0.12
4	<i>TD</i>	Thaw depth	7%	–	0.20
5	<i>Daytime</i>	Day/night	6%	–	–0.36
6	T_{Rim5}	Soil temperature 5 cm, polygon rims	5%	–	–0.35
7	T_{Rim15}	Soil temperature 15 cm, polygon rims	3%	+	0.49
8	<i>U</i>	Wind speed	1%	–	–0.09

for most of the day, about 18 hours on average. Average maximum CO₂ uptake peaked at 9:00 LST ($-3.16 \mu\text{mol}\cdot\text{m}^{-2} \text{s}^{-1}$) and plateaued over an extended period in the middle of the day. Maximum net CO₂ emissions occurred around 0:00 LST, but these observations do not represent ER because the sun was still above the horizon. Methane fluxes had a distinct daily cycle as well, and were negatively correlated with NEE (Pearson's $r = -0.63$). Average maximum daily NME ($49.2 \text{ nmol}\cdot\text{m}^{-2} \text{s}^{-1}$) was double the average minimum ($24.3 \text{ nmol}\cdot\text{m}^{-2} \text{s}^{-1}$) and similar to NEE, there was a mid-day plateau. Figure 5c and 5d shows the daily cycle in late August, just before the power system failed, when there were five to six hours of nighttime per day. Nighttime NEE ($0.95 \mu\text{mol}\cdot\text{m}^{-2} \text{s}^{-1}$) during this period do represent ER. Peak CO₂ uptake occurred at noon and there was no mid-day plateau. The diurnal cycle in NME was still present as well, but the magnitude of emissions decreased substantially.

Net ecosystem exchange

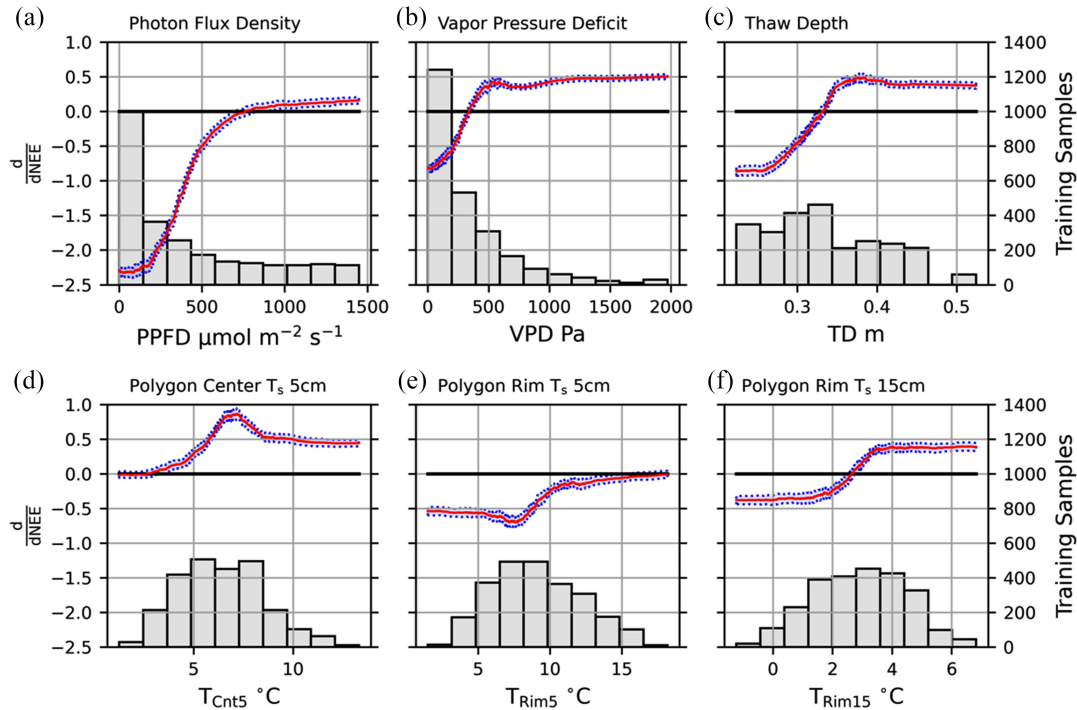
Flux drivers

The model trained on NEE performed very well on the OOB validation data ($r^2 = 0.93$, RMSE = $0.39 \mu\text{mol}\cdot\text{m}^{-2} \text{s}^{-1}$) and performance only dropped slightly compared with the benchmark ($r^2 = 0.95$). Pruning selected 8 inputs for NEE, which are listed in Table 2. *PPFD* is the dominant driver of GPP, and is the primary control over NEE (64% RI). The partial first derivatives of *PPFD* (Fig. 6a) show a strong negative influence that begins to decrease in magnitude at $100 \mu\text{mol}\cdot\text{m}^{-2} \text{s}^{-1}$. The function reaches a minimum around $750 \mu\text{mol}\cdot\text{m}^{-2} \text{s}^{-1}$ (dependent upon the other drivers), above which it has a weak positive influence. The *PPFD* response is modulated by the other drivers, primarily *VPD* (8% RI). It had a strong negative effect over NEE at low *VPD*, that reached an “optimal” value around 340 Pa (Fig. 6b). At higher *VPD*, it was a strong limiting factor over GPP. The response curve of NEE to *PPFD* shows that all else being equal, high *VPD* (1000 Pa) can limit CO₂ uptake by more than $0.5 \mu\text{mol}\cdot\text{m}^{-2} \text{s}^{-1}$ relative to the optimal value (Fig. 7a).

Thaw depth (7% RI) gave the model a seasonal signal that influenced both GPP and ER. Low thaw depths (early season) had a negative influence, NEE trended more negative as vegetation matured (Fig. 6c). The model response shows a minimum around 0.35 m, below this point, all else being equal, NEE trends positive. Figure 7b shows the model response to *TD* for “typical” daytime and nighttime conditions. During daytime, maximum CO₂ uptake can be seen around the timing of the minima identified in Fig. 6c. With radiative inputs fixed to “dark” values, ER decreases steadily from a maximum during the early season, then leveled out around 0.4 m (corresponds to DOY 226) at about $1.0 \mu\text{mol}\cdot\text{m}^{-2} \text{s}^{-1}$. We had limited nighttime NEE observations, and none before DOY 206, so the confidence interval around the modeled ER was broader.

The model identified soil temperature at 5 cm (T_{Cnt5} RI 7%) as the main driver of ER. Above 3 °C, increasing T_{Cnt5} consistently increased ER (Fig. 6d). This was modulated by

Fig. 6. The mean sum of squared derivatives (SSD) for six (a–f) of the input factors for the net ecosystem exchange (NEE) model are shown in red, with a 95% confidence interval shown in blue. Y-axis labels on the left correspond to the SSD values. Also shown (a–f) are histograms (grey bars) of the distribution of the input variables in the training set. The Y-axis labels on the right correspond to the number of training samples (half-hourly observations).

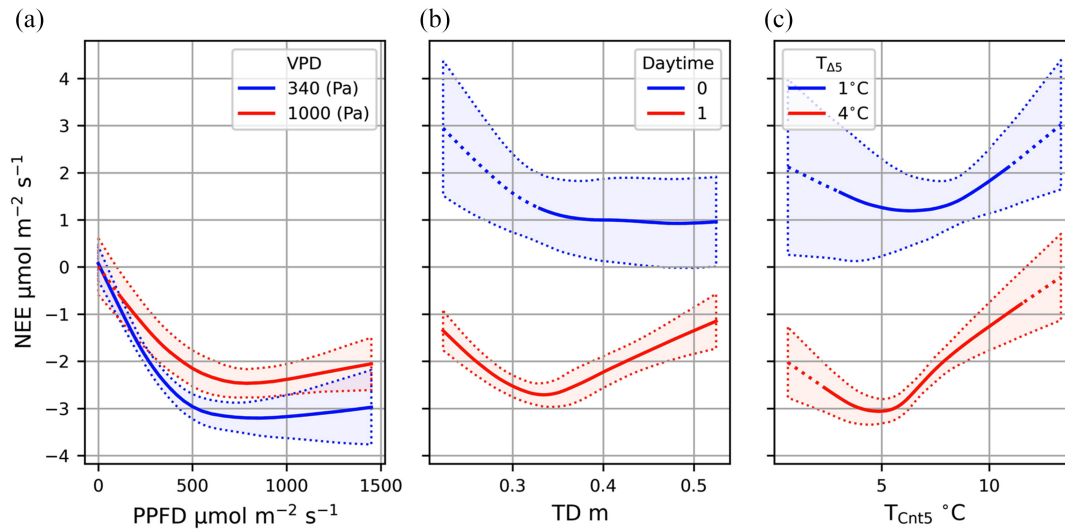


T_{Rim5} (5% RI) and T_{Rim15} (3% RI) that had moderately negative influences at lower temperatures (Fig. 6e and f). At higher temperatures the negative T_{Rim5} influence was negligible and T_{Rim15} became a positive driver. Polygon center and rim temperatures at 5 cm were highly correlated ($r = 0.81$) and moderately to weakly correlated with T_{Rim15} (T_{Cnt5} $r = 0.58$, $T_{Rim5} = 0.19$). Rims were consistently warmer than centers, but the magnitude of the temperature gradient ($T_{\Delta 5} = T_{Rim5} - T_{Cnt5}$) decreased through the study (Fig. 3a). Daily maximum $T_{\Delta 5}$ was in the late afternoon and minimum was in the late night/early morning. The response of NEE to typical late afternoon and late night $T_{\Delta 5}$ is shown in Fig. 7c. There was a strong response to T_{Cnt} at higher temperatures, but the response was muted or even reversed at lower values. Temperatures at 15 cm also had a diurnal signal, but they were much more muted. In the model, T_{Rim15} had more impact on the seasonality of NEE, with higher temperatures at depth indicating increased respiration throughout the soil profile.

Ecosystem respiration

Mean estimated ER was 1.54 ($CI_{95\%} \pm 0.87$) $\mu\text{mol}\cdot\text{m}^{-2}\text{s}^{-1}$, which suggests a mean GPP around 2.14 $\mu\text{mol}\cdot\text{m}^{-2}\text{s}^{-1}$. This is an extrapolation well beyond conditions the model was trained on (see Fig. 8b), so there is more uncertainty around this prediction. The nighttime ER validation statistics for the model ($r^2 = 0.58$, $RMSE = 0.23$ $\mu\text{mol}\cdot\text{m}^{-2}\text{s}^{-1}$) show this method outperformed the Q_{10} response curve ($r^2 = 0.32$, $RMSE = 0.28$ $\mu\text{mol}\cdot\text{m}^{-2}\text{s}^{-1}$) and the best logistic soil temperature curve fit ($T_{Rim2.5}$: $r^2 = 0.45$, $RMSE = 0.26$ $\mu\text{mol}\cdot\text{m}^{-2}\text{s}^{-1}$). The NN does a better job of approximating ER, especially at higher and lower NEE (Fig. 8a). The chamber data gave us increased confidence in our NN derived ER estimate (Fig. 8b). Due to the limited

Fig. 7. Modeled estimated net ecosystem exchange (NEE) under different conditions; unless otherwise specified, all inputs were fixed to their median value. (a) Daytime NEE response to photosynthetic photon flux density (PPFD) at optimal and high vapor pressure deficits (VPD). (b) NEE response to thaw depth (TD) for daytime and nighttime. (c) NEE response to polygon center temperatures at 5 cm daytime and nighttime conditions, with center-rim temperature gradients of 4 °C and 1 °C, respectively. For each plot, the solid lines represent the mean modeled net methane exchange (NME) response, the dotted line is the mean response estimated outside conditions that were actually observed, and the shaded area bounded by the dots is the 95% confidence interval around the estimate.



sample size, here, we report the median and inner quartile range (IQR). Median ER_{Rim} over the two collection days was 2.77 (IQR 2.33 – 4.05) $\mu\text{mol}\cdot\text{m}^{-2}\text{ s}^{-1}$ and was more than double ER_{Cnt} 1.09 (IQR 0.90– 1.39) $\mu\text{mol}\cdot\text{m}^{-2}\text{ s}^{-1}$. Median values between sites also decreased from 1.57 $\mu\text{mol}\cdot\text{m}^{-2}\text{ s}^{-1}$ n DOY 191 to 1.08 $\mu\text{mol}\cdot\text{m}^{-2}\text{ s}^{-1}$ n DOY 233. Our NN derived ER estimate is between median ER_{Cnt} and ER_{Rim} and also showed a decreasing seasonal pattern.

Net methane exchange

The model trained on NME performed reasonably well on the OOB validation data ($r^2 = 0.73$, $RMSE = 6.53\text{ nmol}\cdot\text{m}^{-2}\text{ s}^{-1}$) and performance dropped only slightly compared with the benchmark ($r^2 = 0.74$). Pruning selected 8 inputs for NME, which are shown with their RI in Table 3. The model could not resolve NME as accurately as it could NEE, which is partly due to the smaller number of training samples for NME (1441) vs. NEE (2501). This meant the model had fewer nodes (reduced flexibility) in addition to having less exposure to training data. Additionally, CH_4 fluxes do not have one dominant driver like CO_2 fluxes so the response function is more difficult for the model to resolve.

Net radiation ($RI = 34\%$) had the highest influence, the model derivatives of (Fig. 9a) show a positive influence that begins to decrease in magnitude around $150\text{ W}\cdot\text{m}^{-2}\text{ s}^{-1}$ and reached a maximum around $320\text{ W}\cdot\text{m}^{-2}\text{ s}^{-1}$. Thaw depth was the primary seasonal control ($RI = 12\%$), which had a consistently negative influence (Fig. 9b). The increase in magnitude of negative effect around 0.3 m coincided with the decrease in NME after DOY 202 (Fig. 4b). The influence of R_n in the early and late season is plotted in Fig. 10a. Leaving all other drivers fixed, a TD increase from 0.3 to 0.45 m decreases NME from 10 to 17 $\text{nmol}\cdot\text{m}^{-2}\text{ s}^{-1}$ at low ($0\text{ W}\cdot\text{m}^{-2}\text{ s}^{-1}$) and high ($350\text{ W}\cdot\text{m}^{-2}\text{ s}^{-1}$) R_n respectively. The shape of the curves is similar, but later in the

Fig. 8. (a) Nighttime net ecosystem exchange (NEE) measurements plotted against modeled ecosystem respiration (ER) derived by the neural network (NN) (blue) and logistic temperature response curve fit to $T_{Rim2.5}$ (red). (b) Boxplots of the distribution of flux chamber observations of ecosystem respiration (ER) for polygon centers (ER_{Cnt} , $n = 16$) and rims (ER_{Rim} , $n = 8$) aggregated over the two measurement days. Also shown are the nighttime ER observations from the eddy covariance (EC) system ($n = 186$). For the boxplots, the red line indicates the median, the box represents the inner quartile range (Q1–Q3), the whiskers are 1.5 times the inner quartile range ending at the farthest data point within that interval, and circles represent outliers. Note the Y-axes for a and b are not the same scale.

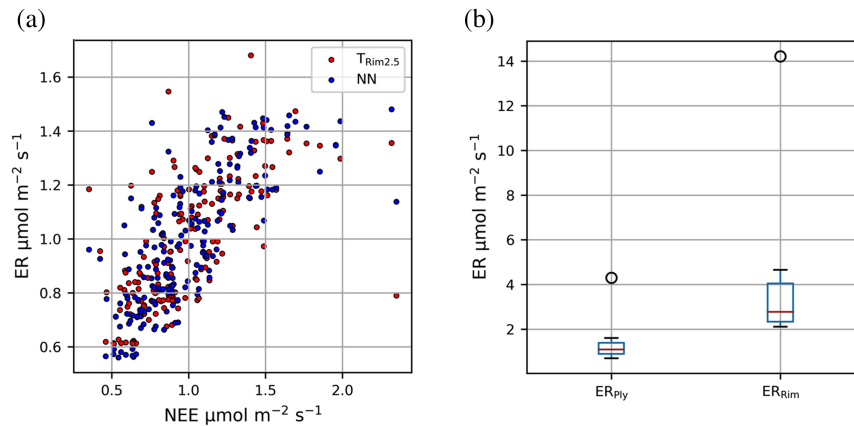


Table 3. Environmental controls over net methane exchange (NME) identified by model pruning, along with their relative influence on the model and their Pearson's correlation coefficient on half-hourly NME.

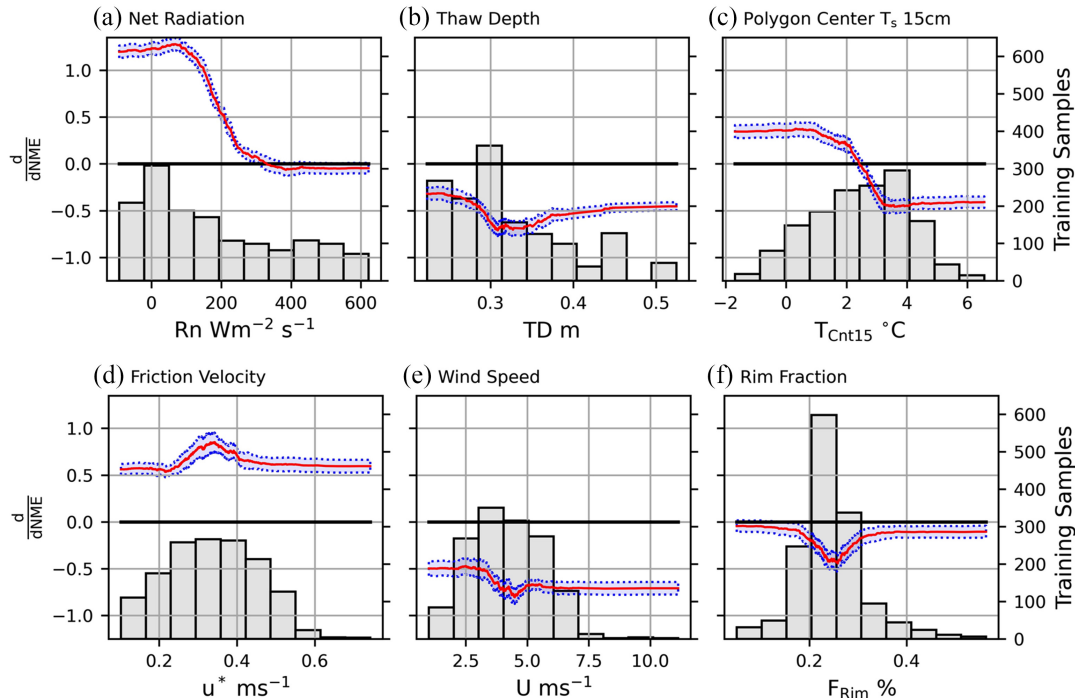
Rank	Symbol	Factor	RI	Sign	r
1	R_n	Net radiation	34%	+	0.66
2	u_*	Friction velocity	20%	+	0.23
3	U	Wind speed	17%	–	0.34
4	TD	Thaw depth	12%	–	–0.46
5	T_{Cnt15}	Soil temperature 15 cm, polygon center	6%	–	–0.58
6	W_{TD}	Water table depth	5%	–	–0.45
7	F_{Rim}	Rim fraction	4%	–	–0.19
8	F_{ply}	Center fraction	2%	–	0.19

season NME does not increase as rapidly with R_n . This would explain the lack of a mid-day plateau seen in the late season (Fig. 5d).

Polygon center temperatures at 15 cm (RI = 6%) had a daily and seasonal signal. The seasonal trend closely mirrored T_{Rim15} (Fig. 3c), peaking in mid-August, then decreasing. The daily maxima and minima occurred around 1:00 LST and 14:00 LST respectively; the mean daily range was greater in the early season (3 °C) than late season (2 °C). This pattern corresponds well with the cycles shown in NME (Figs. 5b and 5d). The derivative of T_{Cnt15} shows a net negative influence on NME, emissions increase until 2.5 °C above which they decrease (Fig. 9c). The parabolic response with to T_{Rim15} is shown at two water table depths (Fig. 10b). Water table depth (RI = 4%) had a modest negative influence over NME. NME decreased as the W_{TD} got closer to the surface, which was unexpected.

The model identified two highly correlated sets of inputs U and u_* ($r^2 = 0.92$) and F_{Rim} and F_{ply} ($r^2 = 0.94$) as well. The wind and footprint variables had combined RIs of 37% and 6%, respectively. The model derivatives of U (negative) and u_* (positive) had inverse effects,

Fig. 9. The mean sum of squared derivative (SSD) for six (a–f) of the input factors for the net methane exchange (NME) model are shown in red, with a 95% confidence interval shown in blue. Y-axis labels on the left correspond to the SSD values. Also shown (a–f) are histograms (grey bars) of the distribution of the input variables in the training set. The Y-axis labels on the right correspond to the input counts for each bin.



indicating that the ratio between the two was important (Fig. 9d and 9e). Friction velocity increases proportionally with wind speed, but the ratio is not fixed. It was on average 8.1% of U with a standard deviation of 1.1%. All else equal, at $U = 5 \text{ m}\cdot\text{s}^{-1}$, a difference of ± 1 std. can result in a $10 \text{ nmol}\cdot\text{m}^{-2} \text{ s}^{-1}$ difference in NME (Fig. 10c).

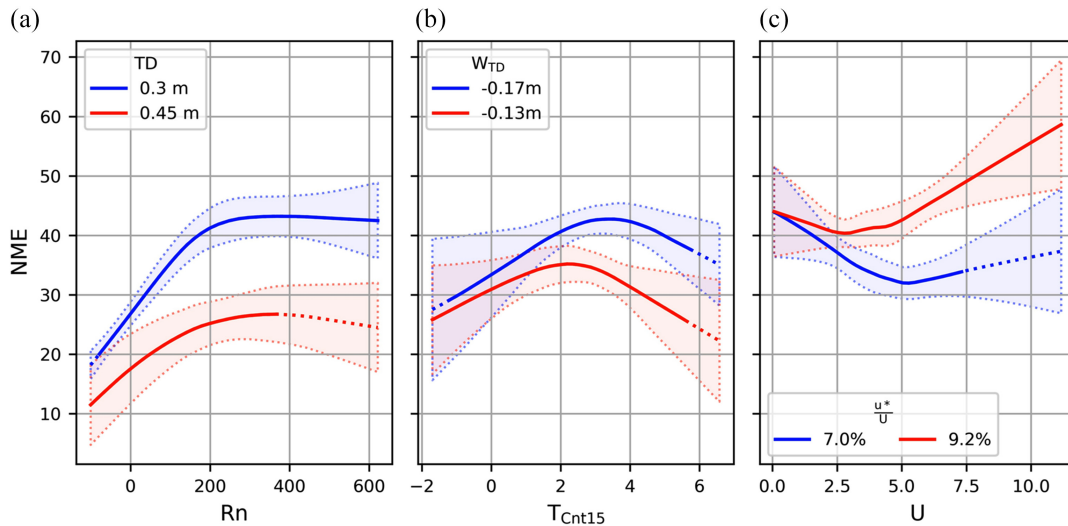
With source area fractions, F_{Rim} increased roughly proportionally with decreasing F_{Ply} with deviations caused by F_{Tro} to a much lesser extent F_{Out} . The effect of changing land cover in the source was generally small, but not insignificant. Supplementary Figure S1¹ shows projections of NME across the range of F_{Rim} and F_{Cnt} with deviations in F_{Rim} to reflect the range of F_{Tro} . Estimating NME over the study period with F_{Rim} and F_{Cnt} fixed to ALF, the model predicts a slightly lower NME 26.6 ($CI_{95\%} \pm 4.3$) $\text{nmol}\cdot\text{m}^{-2} \text{ s}^{-1}$.

Discussion

Flux drivers

NN are ideally suited for modeling the numerous nonlinear relationships that influence carbon fluxes. However, a NN will fit any pattern in a data set, real or artificial, so care must be taken to ensure the results are plausible and repeatable. If a NN is treated as a black box (e.g., Jarvis and Stauch 2006), we have no way of knowing what it is actually doing. Plotting the model output response to specific drivers is beneficial (Moffat et al. 2010; Skeeter et al. 2020), but when working in multidimensional feature space there is no way to assess all possible combinations of drivers. To our knowledge, this is the first study to apply the weights method (Gevrey et al. 2003) to a NN analysis of EC data. This method allowed us to assess each variable's relative influence and visualize the relationship by plotting their

Fig. 10. Modeled estimated net methane exchange (NME) under different conditions. Unless otherwise specified, thaw depth (TD) was set to 0.3 m and all other inputs were fixed to their median value. (a) NME response to net radiation for TD representative of early season (0.3 m) and late season (0.45 m) conditions. (b) NME response to polygon center temperatures (T_{Cnt15}) at two water table depths (W_{TD}). (c) NME wind speeds (U) with friction velocity (u^*) set to 7% and 9.2% of U . For each plot, the solid lines represent the mean modeled NME response, the dotted line is the mean response estimated outside conditions that were actually observed, and the shaded area bounded by the dots is the 95% confidence interval around the estimate.



partial first derivatives, which was especially useful for highly correlated inputs like wind speed and friction velocity.

Spatial variability

In low-center polygonal landscapes, polygon centers are depressed relative to rims. Relief was about 10–20 cm at Fish Island, whereas a site on Samoylov Island in Siberia's Lena Delta had up to 50 cm (Sachs et al. 2010). Anaerobic respiration is favored in the depressed areas, promoting CH_4 production, and inhibiting ER and CH_4 consumption (Lai 2009). Our chamber ER data show higher ER from rims than centers at Fish Island. Similar patterns have been found in chamber ER studies of low-center polygon sites near Barrow (Utqiagvik), AK (Olivas et al. 2011) and Samoylov Island, Siberia (Eckhardt et al. 2019). At Samoylov Island, NME differed by an order of magnitude between centers and rims as well (Sachs et al. 2010). However, rim GPP was higher and lower than center GPP at the Alaskan and Siberian sites, respectively (Olivas et al. 2011; Eckhardt et al. 2019). The rims at Fish Island had more shrub cover than either of the other sites, so we cannot assume the GPP response here would be similar to either the Alaskan or Siberian sites.

At the plot scale, there was significant spatial heterogeneity at Fish Island. The NN analysis indicated polygon rim and center fraction were both relevant for NME, with a combined influence of 6%. Polygon rims had lower NME than centers and both had lower NME than troughs. The source area fractions are not drivers of landscape scale CH_4 per se. Rather they highlight substantial spatial heterogeneity in CH_4 fluxes at Fish Island and indicate location bias had a minor impact on observed NME (Schmid and Lloyd 1999). Following a three-tier site-footprint representative index based on the dominant landcover fraction and chi-square analysis, our site's footprint would be classified as Medium (Chu et al. 2021). Projecting to the ALF shown in Table 1 estimates that landscape scale NME is about $1 \text{ nmol}\cdot\text{m}^{-2} \text{ s}^{-1}$ lower.

This projection can also be used to infer that if permafrost degradation leads to the development of more troughs at Fish Island in the future, landscape scale NME will go up.

For NEE the temperature gradient between rims and centers was relevant, which indicates that microtopography has an effect on landscape scale CO₂ fluxes at Fish Island. Footprint source area inputs were not identified as important drivers (RI > 2.5%) of NEE by the benchmark model, so they were pruned. In the benchmark NEE model, polygon rim (RI = 1.9%) and center (RI = 1.7%) ranked 12th and 14th among the initial 21 inputs, indicating they had little influence on footprint scale NEE compared with the selected drivers. At very low values (e.g., $F_{Rim} < 10\%$), the benchmark model predicts more negative NEE, which supports the chamber observations of reduced ER in polygon centers, but conditions like that accounted for less than 4% of our flux observations. For further comparison, trough fraction ranked 21st (RI = 0.5%) and 9th (RI = 2.4%) in the benchmark NEE and NME models, respectively. The low importance assigned to the source area fractions suggests the placement of the tripod relative to microtopographic features did not have an appreciable impact on the NEE observed.

The resolution of the landscape classification and footprint function (Kljun et al. 2015) may have been limiting factors. However, the average polygon was only 270 m² (~16.5 m across), whereas the 50% and 90% contours for the typical flux footprint were 2300 m² and 6500 m², respectively. Given the relatively small size of the polygons and the regularity with which they repeat across space, the spatial heterogeneity at Fish Island mostly averages out at the footprint scale.

Net ecosystem exchange: flux partitioning

The NN analysis identified PPF_D as the primary control over GPP, and highlighted VPD as the main limiting factor of GPP, which was expected (Aubinet et al. 2012). This relationship has been identified by NN analysis in other studies (Moffat et al. 2010; Skeeter et al. 2020) and has been noted at other wet tundra sites across the Arctic (Kwon et al. 2006; Fox et al. 2008). The model selected polygon center temperatures at 5 cm as the dominant driver, which makes sense given that polygon centers cover the majority of the land area (66%) at the site. It also indicated that the center–rim temperature gradient played an important role in modulating ER. Other studies have found surface temperature rather than soil temperatures to be the primary control over ER in tundra environments (Kutzbach et al. 2007; Runkle et al. 2013). We lacked an observation of surface temperature and would consider adding it in a future study. However, temperatures throughout the upper layers of peat were shown to be strong predictors of ER at a polygonal peatland site in Salluit, Quebec (Gangnon et al. 2017). Further, given the flexibility of NN to account for interactions between variables we are confident this provides a better estimate than soil surface temperature alone could.

When modeling NEE, the network does not inherently differentiate between ER and GPP. Rather it conflates the signals of the two responses into one output. Some studies have trained the NN separately on nighttime and daytime conditions to resolve ER (Papale and Valentini 2003). This approach was not well suited for our site. Instead, we used the *Daytime* variable to give the model the ability to differentiate between night and day without splitting our training data. Skeeter et al. (2020) approximated ER using a NN by setting radiative inputs to “nighttime” values, but they did not use a *Daytime* variable, and their NN underperformed relative to a Q₁₀ curve. We found adding *Daytime* drastically increased the model’s ability to resolve ER, which we support with comparisons to the Q₁₀ and logistic temperature response curves. It also allowed us to estimate ER over the full study period, despite the limited number of nighttime observations, using an artificial “dark” data set.

Our NN derived ER ($1.54 \mu\text{mol}\cdot\text{m}^{-2} \text{ s}^{-1}$) was between the ER_{Cnt} and ER_{Rim} , which gives us confidence in our estimate. Using the half-hourly footprint source area fractions, we can spatially weight our chamber observations. Assuming polygon center/rim distribution outside the LCM mirrors the distribution within it, and ER from troughs is between ER_{Cnt} and ER_{Rim} we get an estimate of 1.62 (IQR1.34 to 2.22) $\mu\text{mol}\cdot\text{m}^{-2} \text{ s}^{-1}$. This is a rough, back of the envelope comparison, but it does further support using this method to estimate ER.

Mean gap-filled NEE, estimated ER and GPP at Fish Island all exceeded ranges observed at a low-center polygon sites in Alaska (Olivas et al. 2011) and Siberia (Eckhardt et al. 2019) using flux chambers. We attribute the differences in GPP to (1) The lower latitude of Fish Island (69°) compared with the Alaskan (71°) and Siberian (72°) sites. (2) More productive vegetation at Fish Island, e.g., *Salix* spp. were absent at the Alaskan and Siberian sites. Differences in ER are attributable to colder soil temperatures and shallower thaw depths (25 cm) and (35 cm) at the Alaskan and Siberian sites respectively (Olivas et al. 2011; Eckhardt et al. 2019).

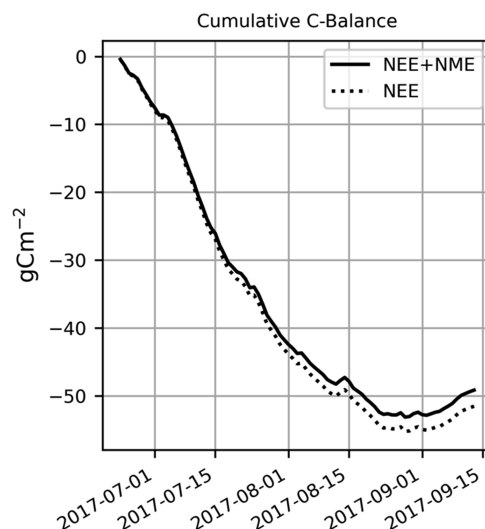
Net methane exchange

There was a significant diurnal cycle in NME throughout the season, and this was identified by the NN selecting R_n as the dominant driver. Many studies in Arctic, subarctic, and peatland sites have not found a distinct diurnal cycles in CH_4 fluxes (Rinne et al. 2007; Sachs et al. 2008; Nadeau et al. 2013; Lee et al. 2017; Rößger et al. 2019b). However, mid-day maxima in NME have been observed at subarctic fens in the Hudson Bay lowlands (Chanton et al. 1992) and Siberia (Veretennikova and Dyukarev 2017). In the Siberian fen, mid-day NME was three times the nighttime values (Veretennikova and Dyukarev 2017), which is even greater than observed at Fish Island. They proposed diurnal temperature variations explain the cycle. We postulate the same is occurring at Fish Island, given the model both polygon center temperatures at 15 cm (T_{Cnt15}) as an auxiliary drivers and the diurnal cycle in T_{Cnt15} . However, we cannot overlook the potential role of plant-mediated transport as another driving factor (Wang and Han 2005). Given the strong positive correlation between NEE and NME, we think this merits further investigation as well.

W_{TD} is known to be a primary determinant of CH_4 production and consumption in peatlands (Kutzbach et al. 2007; Lai 2009). However, Arctic sites with little variation in W_{TD} have found its influence to be negligible (Sachs et al. 2008; Rößger et al. 2019b). At Fish Island, decreasing water table depth had a weak negative influence, which was unexpected. We propose three explanations for this. (1) The range of water table depth was fairly small over the study period. This reasoning was given to explain a similar pattern at a bog in the James Bay lowlands (Nadeau et al. 2013). (2) Data during/after precipitation events when the water table rose rapidly were generally filtered out due to low signal strength (RSSI). Using the unfiltered data, we see strong peaks associated with rising water table, but these signals are unreliable so more studies would be needed to verify this. Gagnon et al. (2017) found precipitation events created conditions that suppressed ER in a polygonal peatland. It is probable that the same thing occurs at Fish Island and leads to elevated NME. (3) Significant loss of data in the second half of the study period means we lack NME observations for many specific combinations of thaw depths and water table levels, limiting the model's ability to resolve the relationship between these drivers. To adequately resolve the influence of water table depth and its interaction with thaw depth, a multi-year data set would be needed.

Perhaps the most interesting finding of our NN analysis is the complex relationship of NME with wind speed (U) and friction velocity (u_*). Spikes in NME associated with high friction velocity have been observed at a low-center polygon site in Siberia (Sachs et al. 2008) and a peatland in the James Bay lowlands (Nadeau et al. 2013). One explanation is that gas

Fig. 11. The cumulative daily carbon (C) balance in $\text{g C}\cdot\text{m}^{-2}$ with and without accounting for net methane exchange (NME).



transfer between open water and the atmosphere increases proportionally to the third power of the windspeed (Sachs et al. 2010; Wanninkhof and McGillis 1999). This likely had some effect because of the ponded troughs within the footprint. However, most of the land area was consistently above the water table. Instead, we frame the hypothesis that high winds and turbulence may enhance pressure pumping (Laemmel et al. 2017; Mohr et al. 2016) that ventilates the aerobic peat layer in the polygon center. We hypothesize that pressure pumping reduces the time CH_4 is subject to methanotrophy within the aerobic layer of peat and, therefore, enhances net CH_4 emissions by transporting it more quickly from the anaerobic layer to the atmosphere. Given that high wind events ventilate CH_4 that would otherwise be consumed, a change in storm frequency paired with an increase in the duration of the snow free season could lead to an increase in emissions from sites like Fish Island, a hypothesis that requires further exploration.

Carbon balance

The low-center polygonal terrain at Fish Island was a net CO_2 sink ($-0.6 \mu\text{mol}\cdot\text{m}^{-2} \text{s}^{-1}$) and a net CH_4 source ($27.7 \text{ nmol}\cdot\text{m}^{-2} \text{s}^{-1}$) during the 2017 study. Overall, NME had a relatively minor impact on net carbon uptake ($-49.5 \text{ g C}\cdot\text{m}^{-2}$) over the 82 day study period (Fig. 11). Our estimate of NME matches well with median daytime NME measured by aircraft (17 to $35 \text{ nmol}\cdot\text{m}^{-2} \text{s}^{-1}$) in vicinity of Fish Island (Kohnert et al. 2017).

A short EC study at Illisarvik, a young drained thermokarst lake basin 17 km to the northeast, is the only observation of NEE available in the scientific literature for comparison in the region (Skeeter et al. 2020). Peak growing season NEE and NME respectively were 1.5 and 0.3 times the magnitude observed at Fish Island. Vegetation at Illisarvik is diverse and basin scale fluxes are not representative of the Fish Island. Compared with chamber fluxes at Illisarvik, ER_{Rim} was most similar to dense *Salix* spp. plots at Illisarvik ($3.4 \pm 0.6 \mu\text{mol}\cdot\text{m}^{-2} \text{s}^{-1}$) whereas ER_{Cnt} was below even bare soil plots ($1.9 \pm 0.3 \mu\text{mol}\cdot\text{m}^{-2} \text{s}^{-1}$). NME was low across vegetation types at Illisarvik, except for sedge plots ($110 \pm 14.7 \text{ nmol}\cdot\text{m}^{-2} \text{s}^{-1}$) that were well above even maximum half-hourly NME ($73 \text{ nmol}\cdot\text{m}^{-2} \text{s}^{-1}$) measured at Fish Island (Skeeter et al. 2020). The only other study in the

region is from manual chamber measurements on high-center polygons near Tuktoyaktuk (Martin et al. 2017). Polygon and wet-trough ER ($1.2 \pm 0.7 \mu\text{mol}\cdot\text{m}^{-2} \text{ s}^{-1}$) were comparable to ER_{Cnt} ; polygon center NME was negligible but wet-trough NME ($150 \pm 236 \text{ nmol}\cdot\text{m}^{-2} \text{ s}^{-1}$) was very high (Martin et al. 2017). No areal fraction for this site was given, so there is no landscape scale estimate to compare between these two types of polygonal terrain.

Lacking more studies of carbon fluxes in the Mackenzie Delta, we can compare current results with Samoylov Island ($72^{\circ}22' \text{N}$, $126^{\circ}30' \text{E}$) in Siberia's Lena River Delta, which has been intensively studied with both EC and chamber methods (Sachs et al. 2008, 2010; Eckhardt et al. 2019; Holl et al. 2019; Rößger et al. 2019a and 2019b). Mean air temperature (-12.8°C) and annual precipitation (321 mm) at Samoylov are colder and wetter than Fish Island (Rößger et al. 2019b). Samoylov Island has two morphological units, a river terrace with low-center polygonal tundra and a floodplain (Kutzbach et al. 2007). The distribution of polygon rims (60%–65%) and centers (35%–40%) and microtopographic relief (up to 50 cm) on the terrace is quite different than at Fish Island, but the vegetation communities present (sedges, mosses, dwarf shrubs), and mean thaw depths (0.49 m) were comparable. Two vegetation communities were at the floodplain site: dense *Salix* spp. up to 1 m tall and *Carex* spp. with dwarf *Salix* spp. Relative to Fish Island, TD (0.7–0.9 m) and W_{TD} (0.4–0.5 m) were deeper. Neither unit is directly analogous to Fish Island, but they can help contextualize our results.

At the floodplain site, averaged over 2014 and 2015, peak growing season and late season NEE respectively were more negative ($-1.77 \mu\text{mol}\cdot\text{m}^{-2} \text{ s}^{-1}$) and positive ($0.77 \mu\text{mol}\cdot\text{m}^{-2} \text{ s}^{-1}$), respectively, than at Fish Island (Rößger et al. 2019a). They attribute the unexpectedly high productivity of this site to regular nutrient input from the spring flood (van Huissteden et al. 2005; Rößger et al. 2019a). At the adjacent river terrace, a 14 year record shows this site is consistently a growing season CO_2 sink, over comparable periods (see Fig. 9 in Holl et al. 2019), net CO_2 uptake at Fish Island between DOY 200 and 234 in 2017 ($-23.1 \text{ g C}\cdot\text{CO}_2 \text{ m}^{-2}$) was greater than all but one year at the terrace site at Samoylov Island. Interannual variability was significant and, in some years, cold season emissions offset growing season uptake (Holl et al. 2019). NME at the floodplain ($15 \text{ nmol}\cdot\text{m}^{-2} \text{ s}^{-1}$) and terrace ($13 \text{ nmol}\cdot\text{m}^{-2} \text{ s}^{-1}$) were well below levels observed at Fish Island (Sachs et al. 2008; Rößger et al. 2019b). These lower methane emissions can partly be explained by the better drainage of the floodplain and difference in microtopography rim/center distribution at the terrace site. Additionally, Fish Island's growing season is warmer; mean July air temperatures of 11.6°C compared to 9.5°C at Samoylov, which may also contribute to higher NME (Holl et al. 2019; NWT Water Resources 2019).

Conclusions

This is the first study to directly and continuously measure growing season NEE and NME within the Mackenzie River Delta by means of eddy covariance. The site, a low-center polygonal peatland at Fish Island was a C sink during the study period with NME having only a minor impact on net C uptake. NME was within the range observed by aircraft in the Northern Mackenzie Delta. Fish Island was a stronger CH_4 source than similar landscapes in the Lena River Delta (Siberia), whereas CO_2 exchange was comparable. We used a NN approach to identify major drivers of NEE and NME at different temporal scales. Variations in light level and temperature were the main controls over diurnal net carbon dioxide uptake, whereas thaw depth and phenology were the main seasonal controls. Methane emissions measured at Fish Island were higher than comparable studies on river delta sites in the Arctic and were influenced by the interaction of numerous of factors including thaw and water table depth, soil temperatures and net radiation. The high

NME and significant interannual variability in flood and climate conditions at this site highlight the need for longer term studies in this region. Additionally, the enhanced NME during high wind events calls for further studies to allow for a process-based understanding of the mechanisms. More research is needed to carefully test the pressure pumping hypothesis and its implications on global-level Arctic CH₄ emissions.

Funding statement

Funding for this study was provided by the Canada Foundation for Innovation (CFI, Grant #33600 to AC and GH) and the National Science and Engineering Research Council of Canada (NSERC) through Discovery Grant RGPIN-2017-03958 (AC), Northern Research Supplement Grant RGPNS-503529 (AC) and Accelerator Supplement RGPAS-507854 (AC).

Data availability statement

The data and code used for post processing, footprint calculations and neural network analysis are available from https://github.com/June-Skeeter/FishIsland_Flux_Analysis.

Acknowledgments

We would like to thank: the staff at the Aurora Research Institute in Inuvik for providing logistical support. Especially Edwin Amos, for the local expertise and invaluable assistance he provided in the field. We would also like to thank Rick Ketler for helping to design and install the floating EC system.

References

- Amiri, B., Dizène, R., and Dahmani, K. 2020. Most relevant input parameters selection for 10-min global solar irradiation estimation on arbitrary inclined plane using neural networks. *Int J Sustain Energy*, **39**(8): 779–803. doi: [10.1080/14786451.2020.1758104](https://doi.org/10.1080/14786451.2020.1758104).
- Anders, U., and Korn, O. 1999. Model selection in neural networks. *Neural Netw*, **12**(2): 309–323. doi: [10.1016/S0893-6080\(98\)00117-8](https://doi.org/10.1016/S0893-6080(98)00117-8) PMID: [12662706](https://pubmed.ncbi.nlm.nih.gov/12662706/).
- Aubinet, M., Vesala, T., and Papale, D. 2012. *Eddy covariance: a practical guide to measurement and data analysis*. Springer, Dordrecht.
- Bosveld, F.C., and Beljaars, A.C.M. 2001. The impact of sampling rate on eddy-covariance flux estimates. *Agri. For Meteorol*, **109**(1): 39–45. doi: [10.1016/S0168-1923\(01\)00257-X](https://doi.org/10.1016/S0168-1923(01)00257-X).
- Briegel, F., Lee, S.C., Black, T.A., Jassal, R.S., and Christen, A. 2020. Factors controlling long-term carbon dioxide exchange between a Douglas-fir stand and the atmosphere identified using an artificial neural network approach. *Ecol Modell*, **435**: 109266. doi: [10.1016/j.ecolmodel.2020.109266](https://doi.org/10.1016/j.ecolmodel.2020.109266).
- Burn, C.R., and Kokelj, S.V. 2009. The environment and permafrost of the Mackenzie Delta area. *Permafrost Periglacial Processes*, **20**(2): 83–105. doi: [10.1002/ppp.655](https://doi.org/10.1002/ppp.655).
- Chanton, J.P., Whiting, G.J., Showers, W.J., and Crill, P.M. 1992. Methane flux from *Peltandra virginica*: Stable isotope tracing and chamber effects. *Global Biogeochem Cycles*, **6**(1): 15–31. doi: [10.1029/91GB02969](https://doi.org/10.1029/91GB02969).
- Christen, A., Jassal, R.S., Black, T.A., Grant, N.J., Hawthorne, I., Johnson, M.S., et al. 2017. Summertime greenhouse gas fluxes from an urban bog undergoing restoration through rewetting. *Mires & Peat*, **17**: 1–24. doi: [10.19189/MaP.2015.OMB.207](https://doi.org/10.19189/MaP.2015.OMB.207).
- Chu, H., Luo, X., Ouyang, Z., Chan, W.S., Dengel, S., Biraud, S.C., et al. 2021. Representativeness of Eddy-Covariance flux footprints for areas surrounding AmeriFlux sites. *Agric For Meteorol*, **301**: 108350. doi: [10.1016/j.agrformet.2021.108350](https://doi.org/10.1016/j.agrformet.2021.108350).
- Dengel, S., Zona, D., Sachs, T., Aurela, M., Jammet, M., Parmentier, F.J.W., et al. 2013. Testing the applicability of neural networks as a gap-filling method using CH₄ flux data from high latitude wetlands. *Biogeosci*, **10**(12): 8185–8200. doi: [10.5194/bg-10-8185-2013](https://doi.org/10.5194/bg-10-8185-2013).
- Desai, A.R., Richardson, A.D., Moffat, A.M., Kattge, J., Hollinger, D.Y., Barr, A., et al. 2008. Cross-site evaluation of eddy covariance GPP and RE decomposition techniques. *Agr. Forest Meteorol.*, **148**(6): 821–838. doi: [10.1016/j.agrformet.2007.11.012](https://doi.org/10.1016/j.agrformet.2007.11.012).
- Derksen, C., Burgess, D., Duguay, C., Howell, S., Mudryk, L., Smith, S., et al. 2019: Changes in snow, ice, and permafrost across Canada. In *Canada's changing climate report*. Edited by E. Bush and D.S. Lemmen. Government of Canada, Ottawa, ON. pp. 194–260.
- Eckhardt, T., Knoblauch, C., Kutzbach, L., Holl, D., Simpson, G., Abakumov, E., and Pfeiffer, E.-M. 2019. Partitioning net ecosystem exchange of CO₂ on the pedon scale in the Lena River Delta, Siberia. *Biogeosci*, **16**(7): 1543–1562. doi: [10.5194/bg-16-1543-2019](https://doi.org/10.5194/bg-16-1543-2019).

- Environment Canada 2016. Tuktoyaktuk Climate Normals 1980–2010. Environment Canada, Ottawa, ON. Available from https://wateroffice.ec.gc.ca/report/historical_e.html?stn=10LC020.
- Environment Canada 2020. Daily water level graph for big lake at Taglu Island (10lc020) (NT), water level and flow.
- Fischer, A. 2015. How to determine the unique contributions of input-variables to the nonlinear regression function of a multilayer perceptron. *Ecol Modell*, **309**, 60–63.
- Fox, A.M., Huntley, B., Lloyd, C.R., Williams, M., and Baxter, R. 2008. Net ecosystem exchange over heterogeneous Arctic tundra: Scaling between chamber and eddy covariance measurements. *Global Biogeochem Cycles*, **22**(2): GB2027. doi: [10.1029/2007GB003027](https://doi.org/10.1029/2007GB003027).
- Frost, G.V., Bhatt, U.S., Epstein, H.E., Myers-Smith, I., Phoenix, G.K., Berner, L.T., et al. 2020. Arctic Report Card 2020: Tundra Greenness. 11 p. doi: [10.25923/46RM-0W23](https://doi.org/10.25923/46RM-0W23).
- Gevrey, M., Dimopoulos, I., and Lek, S. 2003. Review and comparison of methods to study the contribution of variables in artificial neural network models. *Ecol Modell*, **160**(3): 249–264. doi: [10.1016/S0304-3800\(02\)00257-0](https://doi.org/10.1016/S0304-3800(02)00257-0).
- Gagnon, S., Allard, M., and Nicosia, A. 2017. Diurnal and seasonal variations of tundra CO₂ emissions in a polygonal peatland near Salluit, Nunavik. *Canada. Arctic Science*, **4**: 1–15. doi: [10.1139/AS-2016-0045](https://doi.org/10.1139/AS-2016-0045).
- Gautier, D.L., Bird, K.J., Charpentier, R.R., Grantz, A., Houseknecht, D.W., Klett, T.R., et al. 2009. Assessment of undiscovered oil and gas in the Arctic. *Science*, **324**(5931): 1175–1179. doi: [10.1126/science.1169467](https://doi.org/10.1126/science.1169467). PMID: [19478178](https://pubmed.ncbi.nlm.nih.gov/19478178/).
- Holl, D., Wille, C., Sachs, T., Schreiber, P., Runkle, B.R.K., Beckebanze, L., et al. 2019. A long-term (2002 to 2017) record of closed-path and open-path eddy covariance CO₂ net ecosystem exchange fluxes from the Siberian Arctic. *Earth Syst Sci Data*, **11**(1): 221–240. doi: [10.5194/essd-11-221-2019](https://doi.org/10.5194/essd-11-221-2019).
- Hornik, K. 1991. Approximation capabilities of multilayer feedforward networks. *Neural Netw*, **4**(2): 251–257.
- Hugelius, G., Strauss, J., Zubrzycki, S., Harden, J.W., Schuur, E.A.G., Ping, C.-L., et al. 2014. Estimated stocks of circumpolar permafrost carbon with quantified uncertainty ranges and identified data gaps. *Biogeosci*, **11**(23): 6573–6593. doi: [10.5194/bg-11-6573-2014](https://doi.org/10.5194/bg-11-6573-2014).
- Ibrom, A., Dellwik, E., Flyvbjerg, H., Jensen, N.O., and Pilegaard, K. 2007. Strong low-pass filtering effects on water vapour flux measurements with closed-path eddy correlation systems. *Agric For Meteorol*, **147**(3): 140–156. doi: [10.1016/j.agrformet.2007.07.007](https://doi.org/10.1016/j.agrformet.2007.07.007).
- IPCC. 2013. Climate Change 2013: The Physical Science Basis. Contribution of Working Group I to the Fifth Assessment Report of the Intergovernmental Panel on Climate Change. Cambridge University Press. doi: [10.1017/CBO9781107415324](https://doi.org/10.1017/CBO9781107415324).
- Jarvis, A.J., and Stauch, V.J. 2006. A semi-parametric gap-filling model for eddy covariance CO₂-flux time series data. *Global Change Biol*, **12**(9): 1707–1716.
- Khosravi, A., Nahavandi, S., Creighton, D., and Atiya, A.F. 2011. Comprehensive review of neural network-based prediction intervals and new advances. *IEEE Trans Neural Netw*, **22**(9): 1341–1356. doi: [10.1109/TNN.2011.2162110](https://doi.org/10.1109/TNN.2011.2162110). PMID: [21803683](https://pubmed.ncbi.nlm.nih.gov/21803683/).
- Kljun, N., Calanca, P., Rotach, M.W., and Schmid, H.P. 2015. A simple two-dimensional parameterisation for Flux Footprint Prediction (FFP). *Geosci Model Dev*, **8**(11): 3695–3713. doi: [10.5194/gmd-8-3695-2015](https://doi.org/10.5194/gmd-8-3695-2015).
- Knox, S.H., Matthes, J.H., Sturtevant, C., Oikawa, P.Y., Verfaillie, J., and Baldocchi, D. 2016. Biophysical controls on interannual variability in ecosystem-scale CO₂ and CH₄ exchange in a California rice paddy. *J Geophys Res Biogeosci*, **121**(3): 978–1001. doi: [10.1002/2015JG003247](https://doi.org/10.1002/2015JG003247).
- Kohnert, K., Serafimovich, A., Hartmann, J., and Sachs, T. 2014. Airborne measurements of methane fluxes in Alaskan and Canadian tundra with the research aircraft Polar 5, Berichte zur Polar- und Meeresforschung = Reports on polar and marine research, Bremerhaven, Alfred Wegener Institute for Polar and Marine Research, 673, 76 p. doi: [10.2312/BzPM_0673_2014](https://doi.org/10.2312/BzPM_0673_2014).
- Kohnert, K., Serafimovich, A., Metzger, S., Hartmann, J., and Sachs, T. 2017. Strong geologic methane emissions from discontinuous terrestrial permafrost in the Mackenzie Delta, Canada. *Sci Rep*, **7**(1): 1–6. doi: [10.1038/s41598-017-05783-2](https://doi.org/10.1038/s41598-017-05783-2).
- Kohnert, K., Juhls, B., Muster, S., Antonova, S., Serafimovich, A., Metzger, S., Hartmann, J., and Sachs, T. 2018. Toward understanding the contribution of waterbodies to the methane emissions of a permafrost landscape on a regional scale – a case study from the Mackenzie Delta, Canada. *Global Change Biol*, **24**(9): 3976–3989. doi: [10.1111/gcb.14289](https://doi.org/10.1111/gcb.14289).
- Kutzbach, L., Wille, C., and Pfeiffer, E.-M. 2007. The exchange of carbon dioxide between wet arctic tundra and the atmosphere at the Lena River Delta, Northern Siberia. *Biogeosci*, **4**(5): 869–890. doi: [10.5194/bg-4-869-2007](https://doi.org/10.5194/bg-4-869-2007).
- Kwon, H.-J., Oechel, W.C., Zulueta, R.C., and Hastings, S.J. 2006. Effects of climate variability on carbon sequestration among adjacent wet sedge tundra and moist tussock tundra ecosystems. *J Geophys Res Biogeosci*, **111**(G3): G03014. doi: [10.1029/2005JG000036](https://doi.org/10.1029/2005JG000036).
- Laemmel, T., Mohr, M., Schack-Kirchner, H., Schindler, D., and Maier, M. 2017. Direct observation of wind-induced pressure-pumping on gas transport in soil. *Soil Sci Soc Am J*, **81**(4): 770–774. doi: [10.2136/sssaj2017.01.0034n](https://doi.org/10.2136/sssaj2017.01.0034n).
- Lai, D.Y.F. 2009. Methane dynamics in Northern Peatlands: a review. *Pedosphere*, **19**(4): 409–421.
- Lee, J.H.W., Huang, Y., Dickman, M., and Jayawardena, A.W. 2003. Neural network modelling of coastal algal blooms. *Ecol Modell*, **159**(2): 179–201. doi: [10.1016/S0304-3800\(02\)00281-8](https://doi.org/10.1016/S0304-3800(02)00281-8).
- Lee, S.-C., Christen, A., Black, A.T., Johnson, M.S., Jassal, R.S., Kettler, R., et al. 2017. Annual greenhouse gas budget for a bog ecosystem undergoing restoration by rewetting. *Biogeosci*, **14**(11): 2799–2814.
- Liyanaarachchi, V.C., Nishshanka, G.K.S.H., Nimarshana, P.H.V., Ariyadasa, T.U., and Attalage, R.A. 2020. Development of an artificial neural network model to simulate the growth of microalga *Chlorella vulgaris* incorporating the effect of micronutrients. *J Biotechnol* **312**: 44–55. PMID: [32097674](https://pubmed.ncbi.nlm.nih.gov/32097674/).

- Martin, A.F., Lantz, T.C., and Humphreys, E.R. 2017. Ice wedge degradation and CO₂ and CH₄ emissions in the Tuktoyaktuk Coastlands, Northwest Territories. *Arct Sci*, **4**(1): 130–145.
- Mauder, M., and Foken, T. 2004. Documentation and Instruction Manual of the Eddy Covariance Software Package TK2. Universität Bayreuth Abt. Mikrometeorologie. Available from <https://core.ac.uk/download/pdf/33806389.pdf>.
- McDermitt, D., Burba, G., Xu, L., Anderson, T., Komissarov, A., Riensche, B., et al. 2011. A new low-power, open-path instrument for measuring methane flux by eddy covariance. *Appl Phys B*, **102**(2): 391–405. doi: [10.1007/s00340-010-4307-0](https://doi.org/10.1007/s00340-010-4307-0).
- Melesse, A.M., and Hanley, R.S. 2005. Artificial neural network application for multi-ecosystem carbon flux simulation. *Ecol Modell*, **189**(3): 305–314. doi: [10.1016/j.ecolmodel.2005.03.014](https://doi.org/10.1016/j.ecolmodel.2005.03.014).
- Moffat, A.M., Beckstein, C., Churkina, G., Mund, M., and Heimann, M. 2010. Characterization of ecosystem responses to climatic controls using artificial neural networks. *Global Change Biol*, **16**(10): 2737–2749. doi: [10.1111/j.1365-2486.2010.02171.x](https://doi.org/10.1111/j.1365-2486.2010.02171.x).
- Mohr, M., Laemmel, T., Maier, M., and Schindler, D. 2016. Analysis of air pressure fluctuations and topsoil gas concentrations within a Scots Pine Forest. *Atmos*, **7**(10): 125. doi: [10.3390/atmos7100125](https://doi.org/10.3390/atmos7100125).
- Moncrieff, J.B., Massheder, J.M., de Bruin, H., Elbers, J., Friborg, T., Heusinkveld, B., et al. 1997. A system to measure surface fluxes of momentum, sensible heat, water vapour and carbon dioxide. *J Hydrol*, **188**, 589–611. doi: [10.1016/S0022-1694\(96\)03194-0](https://doi.org/10.1016/S0022-1694(96)03194-0).
- Moncrieff, J., Clement, R., Finnigan, J., and Meyers, T. 2004. Averaging, detrending, and filtering of eddy covariance time series. In *Handbook of Micrometeorology*. Edited by X. Lee, W. Massman, and B. Law. Springer, The Netherlands. pp. 7–31.
- Morin, T.H., Bohrer, G., Frasson, R.D., Naor-Azreli, L., Mesi, S., Stefanik, K.C., and Schäfer, K.V.R. 2014. Environmental drivers of methane fluxes from an urban temperate wetland park. *J Geophys Res: Biogeosci*, **119**(11): 2188–2208. doi: [10.1002/2014JG002750](https://doi.org/10.1002/2014JG002750).
- Morse, P.D., Burn, C.R., and Kokelj, S.V. 2012. Influence of snow on near-surface ground temperatures in upland and alluvial environments of the outer Mackenzie Delta, Northwest Territories. *Can J Earth Sci*, **49**(8): 895–913. doi: [10.1139/e2012-012](https://doi.org/10.1139/e2012-012).
- Morse, P.D., and Burn, C.R. 2013. Field observations of syngenetic ice wedge polygons, outer Mackenzie Delta, western Arctic coast, Canada. *J Geophys Res Earth Surf*, **118**(3): 1320–1332. doi: [10.1002/jgrf.20086](https://doi.org/10.1002/jgrf.20086).
- Nadeau, D.F., Rousseau, A.N., Coursolle, C., Margolis, H.A., and Parlange, M.B. 2013. Summer methane fluxes from a boreal bog in northern Quebec, Canada, using eddy covariance measurements. *Atmos Environ*, **81**, 464–474. doi: [10.1016/j.atmosenv.2013.09.044](https://doi.org/10.1016/j.atmosenv.2013.09.044).
- National Research Council Canada, G. of C. N. R. C 2012. Sunrise/sunset calculator. Available from <https://nrc.canada.ca/en/research-development/products-services/software-applications/sun-calculator/>.
- NWT Water Resources 2019. Tagul Automated Weather Station Data (August 2008—July—2019). NWT Water Resources Department. Yellowknife, NWT.
- Olden, J.D., Joy, M.K., and Death, R.G. 2004. An accurate comparison of methods for quantifying variable importance in artificial neural networks using simulated data. *Ecol Modell*, **178**(3): 389–397. doi: [10.1016/j.ecolmodel.2004.03.013](https://doi.org/10.1016/j.ecolmodel.2004.03.013).
- Olivas, P.C., Oberbauer, S.F., Tweedie, C., Oechel, W.C., Lin, D., and Kuchy, A. 2011. Effects of fine-scale topography on CO₂ flux components of Alaskan Coastal Plain Tundra: response to contrasting growing seasons. *Arct Antarct Alp Res*, **43**(2): 256–266. doi: [10.1657/1938-4246-43.2.256](https://doi.org/10.1657/1938-4246-43.2.256).
- Open Drone Map. 2020. Authors ODM – A command line toolkit to generate maps, point clouds, 3D models and DEMs from drone, balloon or kite images. OpenDroneMap/ODM GitHub P. 2020. Available from <https://github.com/OpenDroneMap/ODM>.
- Papale, D., Reichstein, M., Aubinet, M., Canfora, E., Bernhofer, C., Kutsch, W., et al. 2006. Towards a standardized processing of Net Ecosystem Exchange measured with eddy covariance technique: Algorithms and uncertainty estimation. *Biogeosci*, **3**(4): 571–583.
- Papale, D., and Valentini, R. 2003. A new assessment of European forests carbon exchanges by eddy fluxes and artificial neural network spatialization. *Global Change Biol*, **9**(4): 525–535. doi: [10.1046/j.1365-2486.2003.00609.x](https://doi.org/10.1046/j.1365-2486.2003.00609.x).
- Prowse, T.D., Furgal, C., Melling, H., and Smith, S.L. 2009. Implications of climate change for Northern Canada: the physical environment. *AMBIO: A J Human Environ*, **38**(5): 266–271. doi: [10.1579/0044-7447-38.5.266](https://doi.org/10.1579/0044-7447-38.5.266).
- Rinne, J., Riutta, T., Pihlatie, M., Aurela, M., Haapanala, S., Tuovinen, J.-P., et al. 2007. Annual cycle of methane emission from a boreal fen measured by the eddy covariance technique. *Tellus Ser B-Chemical Physical Meteorol*, **59**(3): 449–457. doi: [10.1111/j.1600-0889.2007.00261.x](https://doi.org/10.1111/j.1600-0889.2007.00261.x).
- Rinne, J., Douffet, T., Prigent, Y., and Durand, P. 2008. Field comparison of disjunct and conventional eddy covariance techniques for trace gas flux measurements. *Environ Pollut*, **152**(3): 630–635. doi: [10.1016/j.envpol.2007.06.063](https://doi.org/10.1016/j.envpol.2007.06.063). PMID: [17707112](https://pubmed.ncbi.nlm.nih.gov/17707112/).
- Rößger, N., Wille, C., Holl, D., Göckede, M., and Kutzbach, L. 2019a. Scaling and balancing carbon dioxide fluxes in a heterogeneous tundra ecosystem of the Lena River Delta. *Biogeosci*, **16**(13): 2591–2615. doi: [10.5194/bg-16-2591-2019](https://doi.org/10.5194/bg-16-2591-2019).
- Rößger, N., Wille, C., Veh, G., Boike, J., and Kutzbach, L. 2019b. Scaling and balancing methane fluxes in a heterogeneous tundra ecosystem of the Lena River Delta. *Agricult Forest Meteorol*, **2**: 243–255. doi: [10.1016/j.agrformet.2018.06.026](https://doi.org/10.1016/j.agrformet.2018.06.026).
- Runkle, B.R.K., Sachs, T., Wille, C., Pfeiffer, E.-M., and Kutzbach, L. 2013. Bulk partitioning the growing season net ecosystem exchange of CO₂ in Siberian tundra reveals the seasonality of its carbon sequestration strength. *Biogeosci*, **10**(3): 1337–1349. doi: [10.5194/bg-10-1337-2013](https://doi.org/10.5194/bg-10-1337-2013).

- Sachs, T., Giebels, M., Boike, J., and Kutzbach, L. 2010. Environmental controls on CH₄ emission from polygonal tundra on the microsite scale in the Lena river delta, Siberia. *Global Change Biol*, **16**(11): 3096–3110. doi: [10.1111/j.1365-2486.2010.02232.x](https://doi.org/10.1111/j.1365-2486.2010.02232.x).
- Sachs, T., Wille, C., Boike, J., and Kutzbach, L. 2008. Environmental controls on ecosystem-scale CH₄ emission from polygonal tundra in the Lena River Delta, Siberia. *J Geophys Res-Biogeosci*, **113**, G00A03. doi: [10.1029/2007JG000505](https://doi.org/10.1029/2007JG000505).
- Sarle, W.S. 2014. Comp.ai.neural-nets FAQ, Part 3 of 7: GeneralizationSection—How many hidden units should I use? Comp.Ai.Neural-Nets FAQ. Available from <http://www.faqs.org/faqs/ai-faq/neural-nets/part3/section-10.html>
- Sarle, W.S. 1995. Stopped training and other remedies for overfitting. Proceedings of the 27th Symposium on the Interface of Computing Science and Statistics, 352–360. Available from <http://citeseerx.ist.psu.edu/viewdoc/summary?doi=10.1.1.42.3920>.
- Schmid, H.P., and Lloyd, C.R. 1999. Spatial representativeness and the location bias of flux footprints over inhomogeneous areas. *Agric For Meteorol*, **93**(3): 195–209. doi: [10.1016/S0168-1923\(98\)00119-1](https://doi.org/10.1016/S0168-1923(98)00119-1).
- Schuur, E.A.G., McGuire, A.D., Schädel, C., Grosse, G., Harden, J.W., Hayes, D.J., et al. 2015. Climate change and the permafrost carbon feedback. *Nature*, **520**(7546): 171–179. doi: [10.1038/nature14338](https://doi.org/10.1038/nature14338). PMID: 25855454.
- Skeeter, J., Christen, A., Laforce, A.-A., Humphreys, E., and Henry, G. 2020. Vegetation influence and environmental controls on greenhouse gas fluxes from a drained thermokarst lake in the western Canadian Arctic. *Biogeosci*, **17**(17): 4421–4441. doi: [10.5194/bg-17-4421-2020](https://doi.org/10.5194/bg-17-4421-2020).
- Tarnocai, C., Canadell, J.G., Schuur, E.A.G., Kuhry, P., Mazhitova, G., and Zimov, S. 2009. Soil organic carbon pools in the northern circumpolar permafrost region. *Global Biogeochem Cycles*, **23**(2): GB2023. doi: [10.1029/2008GB003327](https://doi.org/10.1029/2008GB003327).
- Tetko, I.V., Livingstone, D.J., and Luik, A.I. 1995. Neural network studies. 1. Comparison of overfitting and overtraining. *J Chem Inf Model*, **35**(5): 826–833. doi: [10.1021/ci00027a006](https://doi.org/10.1021/ci00027a006).
- Turetsky, M.R., Abbott, B.W., Jones, M.C., Anthony, K.W., Olefeldt, D., Schuur, E.A.G., et al. 2020. Carbon release through abrupt permafrost thaw. *Nat Geosci*, **13**(2): 138–143. doi: [10.1038/s41561-019-0526-0](https://doi.org/10.1038/s41561-019-0526-0).
- van Huissteden, J., Maximov, T.C., and Dolman, A.J. 2005. High methane flux from an arctic floodplain (Indigirka lowlands, eastern Siberia). *J Geophys Res Biogeosci*, **110**(G2): G02002. doi: [10.1029/2005JG000010](https://doi.org/10.1029/2005JG000010).
- Veretennikova, E.E., and Dyukarev, E.A. 2017. Diurnal variations in methane emissions from West Siberia peatlands in summer. *Russ Meteorol Hydrol*, **42**(5): 319–326. doi: [10.3103/S1068373917050077](https://doi.org/10.3103/S1068373917050077).
- Vickers, D., and Mahrt, L. 1997. Quality control and flux sampling problems for tower and aircraft data. *J Atmos Oceanic Technol*, **14**(3): 512–526. doi: [10.1175/1520-0426](https://doi.org/10.1175/1520-0426).
- Wanninkhof, R., and McGillis, W.R. 1999. A cubic relationship between air-sea CO₂ exchange and wind speed. *Geophys Res Lett*, **26**(13): 1889–1892. doi: [10.1029/1999GL900363](https://doi.org/10.1029/1999GL900363).
- Wang, Z.-P., and Han, X.-G. 2005. Diurnal variation in methane emissions in relation to plants and environmental variables in the Inner Mongolia marshes. *Atmos Environ*, **39**(34): 6295–6305. doi: [10.1016/j.atmosenv.2005.07.010](https://doi.org/10.1016/j.atmosenv.2005.07.010).
- Walter Anthony, K.M., Anthony, P., Grosse, G., and Chanton, J. 2012. Geologic methane seeps along boundaries of Arctic permafrost thaw and melting glaciers. *Nat Geosci*, **5**, 419–426. doi: [10.1038/ngeo1480](https://doi.org/10.1038/ngeo1480).
- Webb, E., Pearman, G., and Leuning, R. 1980. Correction of flux measurements for density effects due to heat and water-vapor transfer. *Q J R Meteorolog Soc*, **106**(447): 85–100. doi: [10.1002/qj.49710644707](https://doi.org/10.1002/qj.49710644707).
- Weigend, A.S., and Lebaron, B. 1994. Evaluating neural network predictors by bootstrapping (1994,35; SFB 373 Discussion Papers). Humboldt University of Berlin, Interdisciplinary research project 373: quantification and simulation of economic processes. Available from <https://ideas.repec.org/p/zbw/sfb373/199435.html>
- Wilczak, J.M., Oncley, S.P., and Stage, S.A. 2001. Sonic anemometer tilt correction algorithms. *Boundary Layer Meteorol*, **99**(1), 127–150. doi: [10.1023/A:1018966204465](https://doi.org/10.1023/A:1018966204465).
- Zhang, X., Flato, G., Kirchmeier-Young, M., Vincent, L., Wan, H., Wang, X., et al. 2019: Changes in temperature and precipitation across Canada. Chapter 4 *In* Canada's changing climate report. Edited by E. Bush and D.S. Lemmen. Government of Canada, Ottawa, ON. pp. 112–119.